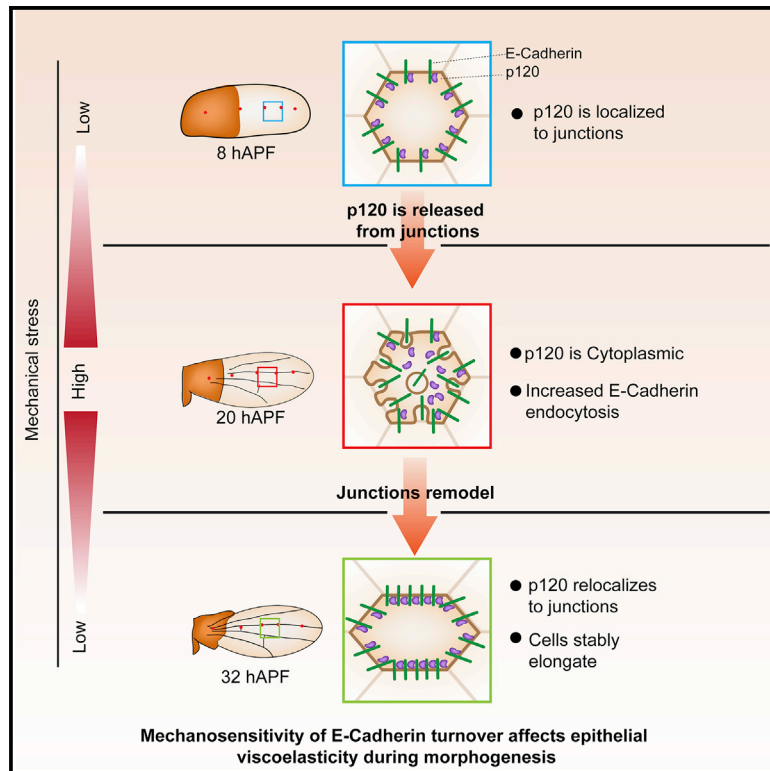# Current Biology

Epithelial Viscoelasticity Is Regulated by Mechanosensitive E-cadherin Turnover

Graphical Abstract

Authors
K. Venkatesan Iyer,
Romina Piscitello-Gómez,
Joris Paijmans, Frank Jülicher,
Suzanne Eaton

Correspondence
iyer@mpi-cbg.de (K.V.I.),
julicher@pks.mpg.de (F.J.),
eaton@mpi-cbg.de (S.E.)

In Brief
How epithelial junctional networks remodel in response to tissue stress is key to morphogenesis. Iyer et al. show that mechanical stress increases endocytic turnover of E-cadherin by depleting the E-cadherin binding protein p120 from cell junctions. This speeds remodeling of the junctional network and decreases cell shape viscosity.

Highlights

- Mechanical stress releases p120-catenin from apical junctions

- Loss of p120-catenin increases endocytic E-cadherin turnover

- Loss of p120 speeds stress-dependent remodeling of the junctional network

- Mechanical stress dependence of E-cadherin turnover sets tissue viscoelasticity

CellPress

Current Biology
Article

CellPress

Epithelial Viscoelasticity Is Regulated by Mechanosensitive E-cadherin Turnover

K. Venkatesan Iyer,[1,2,*] Romina Piscitello-Gómez,[1] Joris Paijmans,[2] Frank Jülicher,[2,4,5,*] and Suzanne Eaton[1,3,4,5,6,*]

[1]Max Planck Institute of Molecular Cell Biology and Genetics, Pfotenhauerstrasse 108, Dresden, Germany
[2]Max Planck Institute for the Physics of Complex Systems, Nöthnitzer Strasse 38, Dresden, Germany
[3]Biotechnologisches Zentrum, Technische Universität Dresden, Tatzberg 47/49, Dresden, Germany
[4]Center for Systems Biology Dresden, Pfotenhauerstrasse 108, Dresden, Germany
[5]Cluster of Excellence Physics of Life, Technische Universität Dresden, 01602 Dresden, Germany
[6]Lead Contact
*Correspondence: iyer@mpi-cbg.de (K.V.I.), julicher@pks.mpg.de (F.J.), eaton@mpi-cbg.de (S.E.)
https://doi.org/10.1016/j.cub.2019.01.021

SUMMARY

Studying how epithelia respond to mechanical stresses is key to understanding tissue shape changes during morphogenesis. Here, we study the viscoelastic properties of the *Drosophila* wing epithelium during pupal morphogenesis by quantifying mechanical stress and cell shape as a function of time. We find a delay of 8 h between maximal tissue stress and maximal cell elongation, indicating a viscoelastic deformation of the tissue. We show that this viscoelastic behavior emerges from the mechanosensitivity of endocytic E-cadherin turnover. The increase in E-cadherin turnover in response to stress is mediated by mechanosensitive relocalization of the E-cadherin binding protein p120-catenin (p120) from cell junctions to cytoplasm. Mechanosensitivity of E-cadherin turnover is lost in p120 mutant wings, where E-cadherin turnover is constitutively high. In this mutant, the relationship between mechanical stress and stress-dependent cell dynamics is altered. Cells in p120 mutant deform and undergo cell rearrangements oriented along the stress axis more rapidly in response to mechanical stress. These changes imply a lower viscosity of wing epithelium. Taken together, our findings reveal that p120-dependent mechanosensitive E-cadherin turnover regulates viscoelastic behavior of epithelial tissues.

INTRODUCTION

How tissue size and shape emerge from the collective behavior of cells is a key question in developmental biology. Time-lapse imaging has revealed that developing tissues reorganize dynamically, indicating fluid-like aspects in their material properties [1–4]. Tissue shape emerges from a dynamic interplay between patterns of active mechanical stress generation and the response of cells and tissues to mechanical stresses [5, 6]. Most studies have focused on how tissue dynamics results from patterns of cellular force generation organized by biochem-

ical signals [7–9]. However, the possible mechanical responses of tissues [10], and how these responses are deployed during development, remain largely unclear.

The response of soft materials, like tissues, to mechanical stress depends on their material properties, which are typically viscoelastic [11–13]. Elastic materials deform in response to mechanical stress and return to their original shape when stress is removed. Viscous materials behave like fluids—they relax mechanical stresses by remodeling their internal structure and do not return to their original shape after deformation. Viscoelastic materials combine both behaviors—they are elastic over short timescales and viscous at longer timescales [14]. What mechanisms determine the viscoelastic properties of developing tissues? Studying such mechanisms is key to understanding stress-dependent tissue shape changes during development.

The *Drosophila* pupal wing is an ideal system to study how epithelial tissues respond to mechanical stress during morphogenesis [2, 3]. From 16 h after puparium formation (hAPF), the wing blade epithelium deforms in response to anisotropic proximal-distal (PD)-oriented tissue stresses. These stresses develop during contraction of the more proximal hinge region. Stresses develop because the wing blade is connected along its margin to an overlying cuticle through an extracellular matrix protein called Dumpy [3, 15, 16]. Over about 20 h, the wing blade extends along the PD axis and narrows in the anterior-posterior (AP) axis. Decomposing the overall tissue deformation into contributions stemming from different cellular processes revealed that oriented cell divisions, cell rearrangements (T1 transitions), and cell shape changes all contribute to this tissue shape change [3, 17, 18]. We used both laser ablation and genetic perturbations to show that PD-oriented tissue stresses are necessary for both PD cell elongation and PD-oriented cell rearrangements [3]. One key missing piece of information is the extent to which the combination of cell mechanics and cell rearrangements relax the stresses generated by hinge contraction. Furthermore, the molecular mechanisms that underlie stress-dependent changes in cell shape and cell rearrangements are not known.

Cell shape changes and rearrangements during morphogenesis involve the remodeling of the apical junctional network [19, 20]. E-cadherin is a core component of *adherens* junctions that not only mediates adhesion between cells but also regulates the linkage of adhesive complexes to the underlying acto-myosin cytoskeleton and controls cytoskeletal dynamics
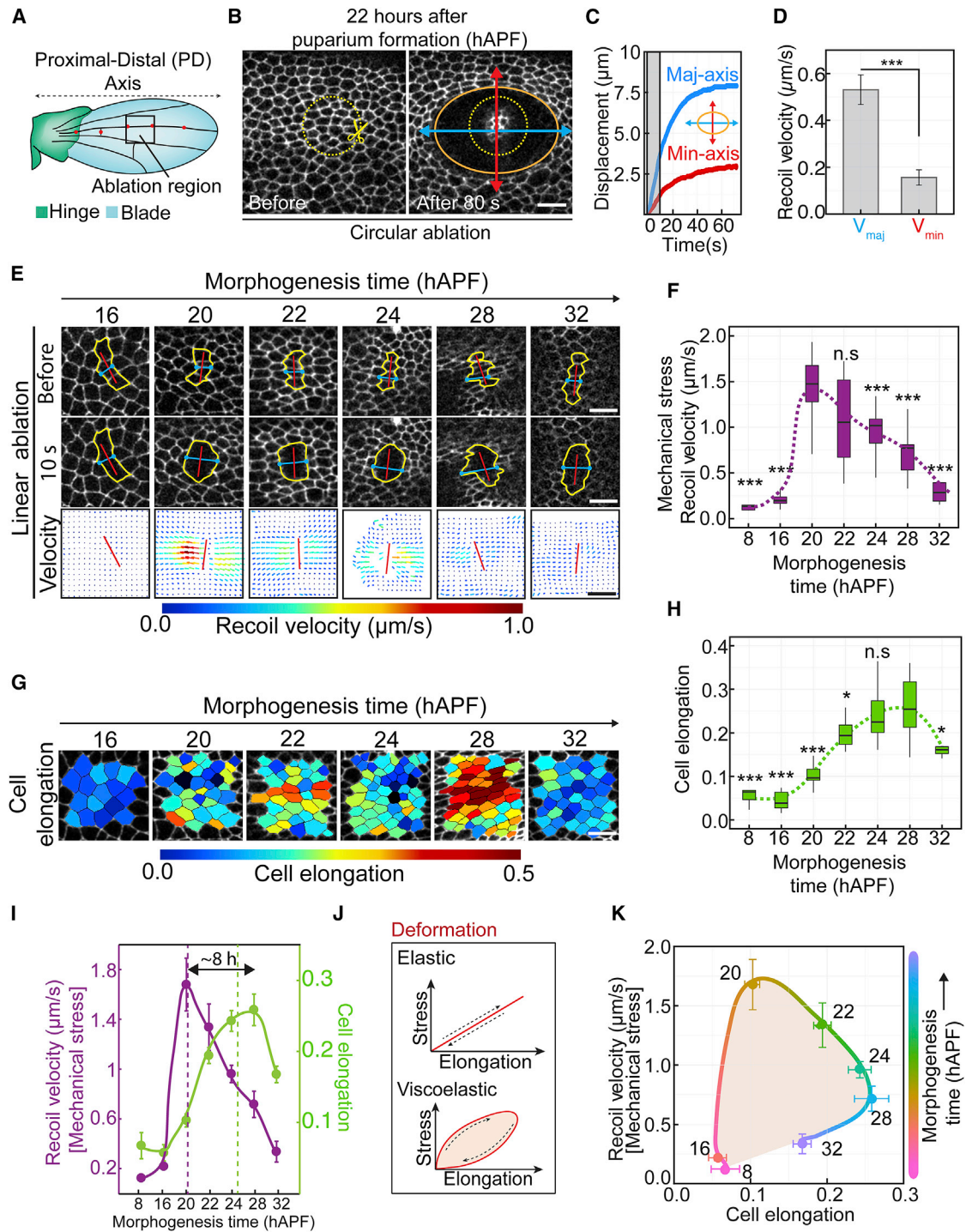
Figure 1. Epithelial Tissue Undergoes Viscoelastic Deformation during Morphogenesis

(A) Schematic of the *Drosophila* pupal wing epithelium showing the hinge (green) and blade (blue) regions. Red dots represent sensory organs. Laser ablations were performed in the region shown in black region of interest (ROI).

(B) Images of the region of the pupal wing shown in (A) before and 80 s after circular ablation of 20 μm diameter at 22 hAPF. Yellow-dotted ROI (with scissors) represents the ablated circle. Orange ellipse shows the size of the ablated region 80 s after ablation. Blue and red double-sided arrows show the expansion along major and minor axes of the ellipse. Scale bar, 10 μm.

(C) Displacement versus time graph for the circular ablation. Blue and red curves represent displacement along the major and minor axis of the ellipse, respectively. Grey region represents the region of the curve used for estimating the initial recoil velocity.

(D) Initial recoil velocities along the major and minor axes of the ellipse. Error bars, SEM. ***p < 0.0001 (n ≥ 5 wings). The p values are estimated by Student's t test.

(legend continued on next page)

[20, 21]. Most studies in cultured cells have highlighted how mechanical stress increases the linkage of E-cadherin to the actin cytoskeleton and promotes adhesion. α-catenin, which is recruited to the E-cadherin cytoplasmic tail through β-catenin, unfolds under stress and binds to actin filaments [22]. α-catenin also recruits another mechanosensitive protein, vinculin, which upon unfolding enhances actin binding and actin polymerization [23, 24]. However, results in MDCK cells suggest that stress can also destabilize E-cadherin-dependent adhesions [25]. This appears to involve internalization of E-cadherin complexes, but the mechanisms underlying stress-dependent internalization are not known. Such mechanisms could be particularly relevant during morphogenesis of the pupal wing, where stress induces remodeling of the junctional network. Therefore, they may also be important for the understanding of viscoelastic behaviors of such tissues.

Here, we show that the *Drosophila* wing blade exhibits viscoelastic behaviors upon deformation in response to stress induced by hinge contraction. Both cell rearrangements and changes in cell mechanics contribute to the viscosity of the wing epithelium. We provide evidence that mechanical stresses destabilize E-cadherin complexes and elevate endocytic turnover of E-cadherin in the wing blade. We have identified that p120-catenin, a protein that binds to the E-cadherin tail, is a part of a mechanotransduction pathway. When mechanical stress is high, p120 is released from *adherens* junctions and re-associates with junctions as stress relaxes. Mechanosensitivity of E-cadherin turnover depends on the binding p120-catenin (p120) to E-cadherin. In the *p120* mutants, E-cadherin turnover no longer responds to tissue stress and remains high even when stresses relax. The apparent viscosity of the wing epithelium is reduced by loss of p120. Our work reveals that mechanotransduction through p120 regulates the turnover of E-cadherin and thereby tunes the viscoelastic properties of the wing epithelium.

RESULTS

Epithelial Tissue Undergoes Viscoelastic Deformation during Morphogenesis

The first step toward studying the viscoelastic properties of the wing is to measure the time dependence of mechanical stress in the wing during morphogenesis. Focusing on a region between the 3rd and 4th longitudinal veins, we used two laser ablation approaches to estimate the orientation and magnitude of mechanical stress at different times of development (Figure 1A). To reveal stress orientation, we performed circular laser ablations and monitored the deformation of the ablated shape over time (Figure 1B). Circular ablations deformed into ellipses whose major axes were predominantly aligned with the PD axis of the wing, confirming that mechanical stress remains aligned with the PD axis throughout morphogenesis (Figures 1C and 1D). These experiments also suggested that the magnitude of mechanical stress first increases and then decreases over time (Figures S1A–S1D). The initial velocity of retraction is the best proxy for stress [26]. However, because of the time required to perform circular cuts, it is difficult to measure this velocity for such cuts. We therefore performed linear ablations orthogonal to the PD axis to measure the initial velocity of retraction at different times (Figure 1E). These experiments revealed that stress increases dramatically between 16 and 20 hAPF and then gradually relaxes back to its initial low value by 32 hAPF (Figure 1F). The fact that stress relaxes during wing morphogenesis indicates that the wing blade tissue has viscous material properties. Our analysis suggests that not only cell rearrangements but also changes in preferred cell shape contribute to stress relaxation during morphogenesis (Figures 1G and 1H).

We took advantage of the increase and decline of mechanical stress during wing tissue deformation to investigate tissue viscoelastic properties. Viscoelasticity of soft materials is typically characterized by studying the relationship between periodic material deformations and corresponding oscillating stress. An elastic material undergoes instantaneous deformation that is in phase with the applied stress oscillation. A viscous material shows a time delay between the deformation and applied stress such that deformation and stress are 90 degrees phase shifted. Viscoelastic materials show a response with an intermediate phase shift. Measuring deformation during mechanical loading and unloading permits one to plot a mechanical stress-deformation curve, which provides information about the phase relation between deformation and stress and thus the viscoelasticity of the tissue (Figure 1J). To study the relationship between cell deformation and mechanical stress, we measured the average cell elongation in the region around the ablation prior to ablation.

(E) Images showing linear laser ablation in the region of pupal wing shown in (A) during morphogenesis. Red dotted line represents the 7-μm ablation. Yellow ROI represents the outline of the cells around the ablation line, before and 10 s after ablation. Velocity image shows the recoil velocity profile with velocity vectors originating from the site of ablation. The length and color of the vectors represents the magnitude of the recoil velocity. Scale bars, 5 μm.

(F) Boxplot shows the recoil velocity (proxy for mechanical stress) during different stages of the wing morphogenesis. Error bars, SEM. ***p < 0.0001. p values were estimated by Student's t test with respect to 20 hAPF (n ≥ 5 wings in each case).

(G) Color-coded images showing cell elongation at different stages of wing morphogenesis for the same region as laser ablation. Scale bar, 5 μm.

(H) Boxplot shows the cell elongation during wing morphogenesis. Error bars, SEM. *p < 0.05; ***p < 0.0001. p values were estimated by Student's t test with respect to 20 hAPF (n ≥ 5 wings in each case).

(I) Cell elongation (green) and mechanical stress (magenta) during wing morphogenesis. Filled circles show the experimental data, and the line represents temporal evolution of cell elongation and mechanical stress. The peak of mechanical stress and cell elongation are separated by an 8-h time delay. Error bars, SEM.

(J) Schematic showing the relationship between stress and elongation during cyclic stretching of an elastic and viscoelastic material.

(K) Mechanical stress versus cell elongation graph during pupal wing morphogenesis. Filled circles represent experimental data, color coded for the time of morphogenesis. Numbers beside the points show the stage of wing morphogenesis (in hAPF). The color-coded smooth curve represents the temporal evolution of mechanical stress and cell elongation during morphogenesis. The color codes correspond to morphogenesis time in hAPF. The area under the smooth curve (peach) shows the hysteresis in the process and corresponds to the dissipation due to viscoelastic deformation. Error bars, SEM.
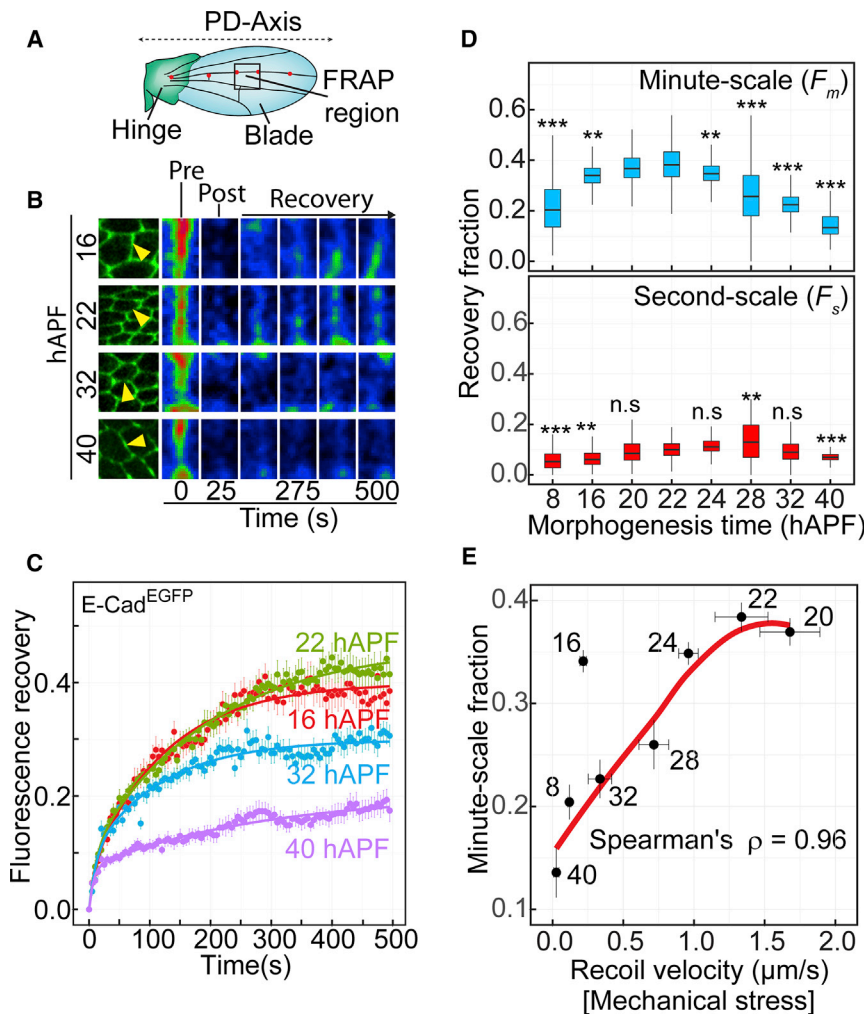
See also Figure S1.

Figure 2. E-cadherin Turnover during Morphogenesis Is Mechanosensitive

(A) Schematic shows that FRAP experiments were performed in the same region of the pupal wing where laser ablations were performed.

(B) Time-lapse images from FRAP time series of E-cad at 16, 22, 32, and 40 hAPF. Yellow arrows show the junctions that are bleached. Time series images show the pre- and post-bleach images and the recovery over 500 s. Images are color coded for intensity.

(C) FRAP curves for E-cad. Solid line shows the double exponential fit. Error bars, SEM (n $\geq$ 40 junctions in each case).

(D) Boxplot shows minute-scale, F_m (blue), and second-scale, F_s (red), recovery fractions for E-cad. Error bars, SEM. **p < 0.01 and ***p < 0.001. p values are estimated for F_m and F_s at all time points with respect to 22 hAPF, and n.s. indicates that the differences are not significant (n $\geq$ 40 junctions in each case). The p values are estimated by Student's t test.

(E) Scatterplot between mechanical stress and minute-scale recovery fraction (F_m). Color of the points and the numbers beside the points represent time of morphogenesis in hAPF. Solid red line is the locally weighted smoothing of the scatterplot with 16 hAPF excluded. A Spearman's correlation coefficient, ρ = 0.96, with a false discovery rate of 2 × 10^{-4} is observed between recoil velocity and minute-scale fraction.

See also Figure S1 and Table S1.

Cells elongate in the PD axis until 28 hAPF and then partially relax their shape as cell rearrangements help to relax stress (Figures 1G and 1H). Plotting both average cell elongation and mechanical stress as a function of time revealed a delay of 8 h between the peaks of stress and cell deformation (Figure 1I), suggesting that cells themselves exhibit viscoelastic behaviors. The viscous component is also highlighted by the large area enclosed by the stress-cell deformation curve (Figure 1K). This suggests that cell shapes are not only elastic but also exhibit viscosity.

E-cadherin Turnover during Morphogenesis Is Mechanosensitive

To begin the investigation of molecular mechanisms that underlie the viscoelastic properties of the wing epithelium, we examined the rate of E-cadherin turnover during morphogenesis. To do so, we used E-cadherin::GFP (E-cad) to perform fluorescence recovery after photobleaching (FRAP) measurements at different times during pupal morphogenesis. We photobleached a single cell junction in the same region and at the same times at which we had measured mechanical stress using laser ablation (Figure 2A) and then quantified the recovery of fluorescence over a period of 500 s (Figures 2B and 2C). Recovery over this time

period was well described by a double exponential function (Table S1),

$$I_{Frap}(t) = F_s\left(1 - e^{-t/\tau_s}\right) + F_m\left(1 - e^{-t/\tau_m}\right), \quad \text{(Equation 1)}$$

where $I_{Frap}(t)$ is the intensity of the junction at time t, τ_s and τ_m are two timescales of recovery, and F_s and F_m are the corresponding recovery fractions. The timescale τ_s ranged from 10 to 50 s and is referred to as the second timescale (Figure S1E). F_s is the corresponding second-scale recovery fraction. The timescale τ_m varied between 2 and 8 min and is referred to as the minute timescale (Figure S1E). F_m is the corresponding minute-scale recovery fraction. In longer videos, an additional recovery process was observed, revealing a third timescale on the order of ∼2 h (Figure S1G). We refer to this fraction as the immobile fraction. The proportions of the immobile fraction and minute timescale fraction F_m changed during pupal wing morphogenesis as stresses build up and relax (Figure S1F). The minute timescale fraction already increases at the expense of the immobile fraction between 8 and 16 hAPF, before significant mechanical stress emerges. As stresses due to hinge contraction increase, F_m is elevated further, peaking between 20 and 22 hAPF. Then,
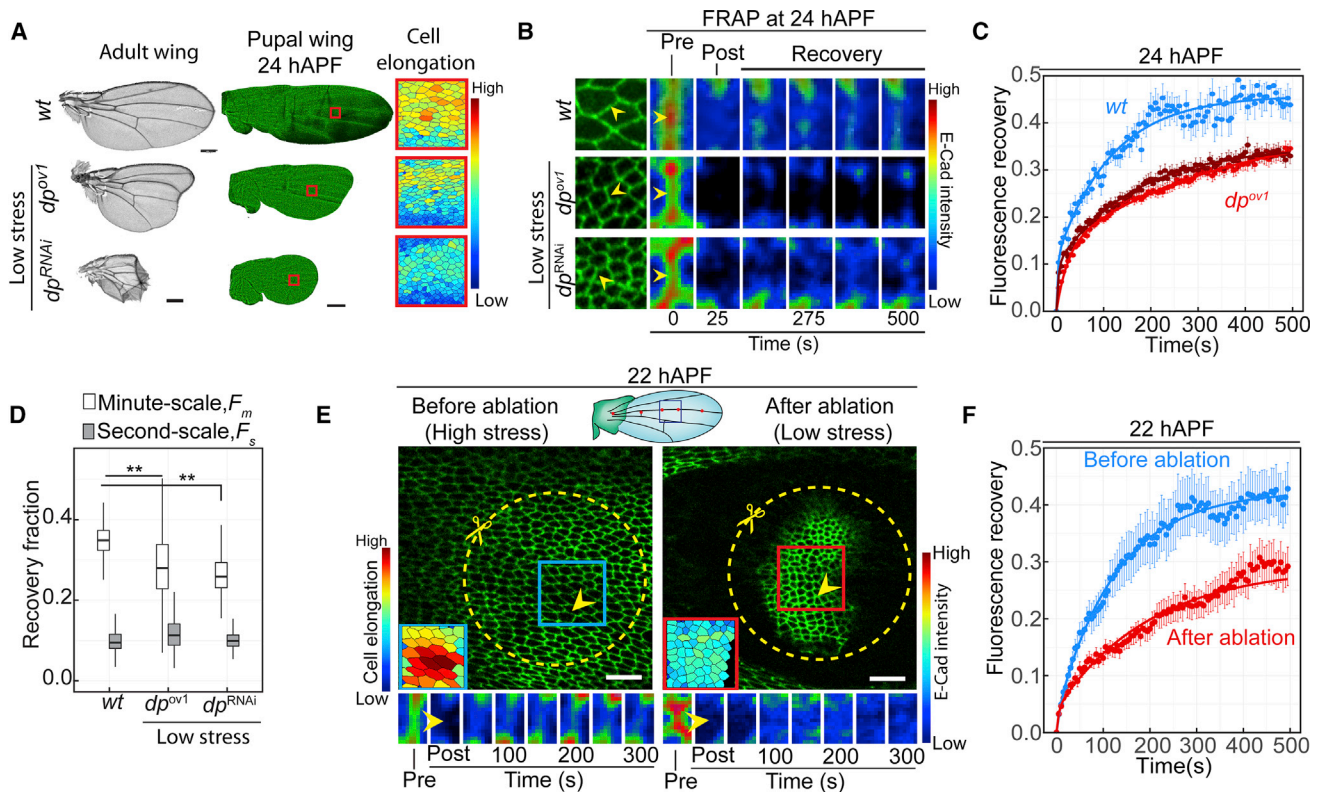
Figure 3. Mechanical Stress Regulates E-Cadherin Turnover

(A) Adult wings (left panel) and 24 hAPF pupal wings (middle panel) of wild-type (WT), dp^{ov1}, and dp^{RNAi}. Scale bars in left panel, 200 μm. Scale bar in middle panel, 100 μm. Red ROI represents the region for which color-coded cell elongation is shown in the right panel.

(B) Images show a small region of the wing where FRAP was performed. Yellow arrows show the bleached junctions. Time-lapse images show the pre- and post-bleach frames, followed by recovery of fluorescence.

(C) Fluorescence recovery curves for WT (blue), dp^{ov1} (red), and dp^{RNAi} (dark red) at 24 hAPF. Solid lines represent double exponential fits. Error bars, SEM (n ≥ 65 junctions in each case).

(D) Boxplots show minute-scale (white) and second-scale (gray) recovery fractions for wt, dp^{ov1}, and dp^{RNAi}. **p < 0.001 (n ≥ 65 junctions in each case). The p values are estimated by Student's t test.

(E) The schematic of the pupal wing shows the region where ablation was performed (black ROI in the wing). Yellow dotted ROI (with scissors) shows the ablated region. Bottom insets show color-coded cell area before ablation (blue ROI) and after ablation (red ROI). Scale bars, 10 μm. Bottom panels show the intensity color-coded time-lapse images of fluorescence recovery of the bleached junctions shown by yellow arrow, before and after ablation.

(F) Fluorescence recovery curves before (blue) and after (red) ablation. Error bars, SEM (n ≥ 15 junctions in each case).

See also Figures S2 and S3.

F_m gradually decreases between 22 and 40 hAPF, as stresses relax (Figure 2D). In contrast, the second scale fraction F_s varies much less during morphogenesis (Figure 2D). Plotting the minute scale fraction F_m as a function of mechanical stress highlights the positive relationship between stress and F_m (Figure 2E) but also suggests that this fraction of E-cadherin is higher at 16 hAPF than that would be expected if it were completely stress dependent. The non-linear Spearman's correlation coefficient between stress and F_m is 0.96 when 16 hAPF value is not included but 0.9 when it is included (Figure 2E). The higher than expected turnover of E-cadherin at 16 hAPF may indicate that an additional stress-independent mechanism also promotes turnover at this time. Alternatively, E-cadherin turnover may respond somewhat differently to increasing and decreasing mechanical stress. These observations suggest that minute-scale recovery fraction and immobile fraction are mechanosensitive, whereas the second-scale fraction is insensitive to mechanical stress (Figure S1H).

Mechanical Stress Regulates E-cadherin Turnover

We have shown that change in mechanical stress during pupal wing morphogenesis correlates strongly with changes in E-cad turnover. One explanation for this correlation is that mechanical stress directly regulates this process. Alternatively, mechanical stress and E-cad turnover might be controlled independently during morphogenesis. To resolve these possibilities, we used both genetic and physical means to reduce mechanical stress at a time when it is normally high and then examined E-cad turnover. First, we used the hypomorphic dumpy mutant, dp^{ov1} [16]. In this mutant, matrix connections between the cuticle and the distal tip of the wing are depleted, and these wings therefore never develop the same magnitude of mechanical stress as wild-type wings (Figure S2E). This leads to reduced cell area and cell elongation (Figures 3A, S2C, and S2D). We also reduced the levels of Dumpy in the entire wing by expressing double-stranded RNA (dsRNA) of Dumpy in the wing—dp^{RNAi} [15]. This produces stronger adult phenotypes and affects cell elongation

even more dramatically than dp^{ov1} (Figures 3A and S2C). We performed FRAP on single junctions of wild-type, dp^{ov1}, and dp^{RNAi} wings at 24 hAPF, when *dumpy* mutant wing blades have already retracted from the cuticle (Figures 3B, 3C, and S2A). Both Dumpy perturbations strongly reduce E-cad turnover, specifically the minute-scale recovery fraction (F_m), although the second-scale fraction (F_s) is not affected (Figures 3C, 3D, and S2F). These FRAP experiments suggest that mechanical stress increases the turnover of E-cad.

To investigate the influence of acute reduction in mechanical stress on E-cad turnover, we performed FRAP experiments in wild-type wings before and after a circular laser ablation at 22 hAPF, when the blade is under high mechanical stress (Figures 3E and S3A). After the first FRAP measurements, we ablated a circle with a radius of 20 μm around the analyzed region. This isolated a small tissue island from the surrounding tissue (Figure 3E). Within 10 min of ablation, cells in the tissue island contracted their apical cross-section and became less elongated (Figures 3E and S3B), indicating that the laser ablation rapidly relieves mechanical stress in the tissue island. We then performed a second FRAP analysis within this isolated region. After ablation, F_m decreased by 47% ± 5% (Figures 3F and S3D). In contrast, F_s was not affected (Figure S3E). Thus, although minute-scale fraction of E-cad responds rapidly to changes in mechanical stress, second-scale fraction is independent of stress. We observed that E-cad turnover was consistently high in early stage (16 hAPF) and did not increase further with increasing mechanical stress (Figures 2C–2E). Thus, we wondered to what extent mechanical stress-dependent mechanisms contributed to E-cad turnover at this stage. To investigate this, we measured E-cad turnover at 16 hAPF before and after generating an isolated tissue island by circular laser ablation (Figures S3D and S3E). In contrast to 22 hAPF, only 26% ± 5% of F_m was stress dependent (Figures S3E and S4F). This revealed that, at 16 hAPF, a significant but smaller fraction of F_m is dependent on mechanical stress. However additional active mechanisms could also promote E-cad turnover at this stage. Taken together, these data show that the mechanical stress regulates the turnover of E-cad during wing morphogenesis.

We wondered whether stress-dependent turnover is specific to *adherens* junctions or whether stress might also act at septate junctions to increase protein turnover. Septate junctions are located approximately 3 μm below the *adherens* junctions (Figure S3G) and are thought to inhibit the flux of small molecules and ions between epithelial cells [27]. We performed laser ablations at the level of septate junctions, visualized using neuroglian::EGFP (Nrg) (Figure S4H). Interestingly, the septate junction region is under significantly less mechanical stress than the *adherens* junction region containing E-cad (Figure S3I). Furthermore, FRAP analysis indicated that Nrg turns over much more slowly than E-cad and that turnover does not change during pupal wing remodeling (Figures S3J and S3K). Thus, E-cad and the *adherens* junction region appear to be specialized sites of mechanical stress sensing and response.

Membrane Trafficking Contributes to the Minute-Scale Recovery of E-cadherin

Next, we asked what cell biological mechanisms contribute to the minute-scale and second-scale recovery fractions. E-cad

fluorescence could in principle recover either through the vesicular delivery of new E-cad from the cytoplasm or by lateral diffusion within the membrane [28]. To distinguish the relative contributions of each process, we used two different approaches to perform FRAP at 22 hAPF. In the first approach, we bleached the junction of interest (JOI) and the neighboring junctions connected to JOI (Figure 4A, ii), depleting the junctional pool of E-cad and ensuring that the JOI could recover only from cell-internal stores and not from lateral diffusion from other membranes. Comparing these results to those of single-junction FRAP (Figure 4A, i), we observed that F_s was significantly reduced, whereas F_m only showed a small change. In the second approach, we bleached the JOI and large cytoplasmic regions of the cells belonging to JOI, ensuring that internal stores of E-Cad are not available for E-cad fluorescence recovery (Figure 4A, iii). In these experiments, we observed that the F_m was significantly reduced, whereas the F_s only showed a small decrease. Thus, we conclude that lateral diffusion on the membrane contributes to the second-scale recovery fraction (F_s) and this process is mechanical stress independent, whereas membrane trafficking from internal stores contributes to the mechanical-stress-dependent minute-scale recovery fraction (F_m).

Mechanical Stress Modulates Endocytosis-Mediated E-cadherin Turnover

To investigate whether the membrane trafficking fraction (F_m) of E-cad is derived from endocytosis, we examined the temperature-sensitive dynamin mutant *shibire*^{ts} (shi^{ts}), in which dynamin-dependent endocytosis is blocked above the restrictive temperature of 34°C [29–31] (Figures 4B and S4A). Upon shifting shi^{ts} mutant wings at 22 hAPF, from 25°C to 34°C for 10 min, mean fluorescence of E-cad increased at cell junctions, suggesting that E-cad is normally continuously removed from cell junctions by dynamin-dependent endocytosis (Figure S4B). To ask how blocking dynamin-dependent endocytosis influenced the minute-scale and second-scale recovery fractions, we performed FRAP on wild-type and shi^{ts} mutant wings at 22 hAPF, either at 25°C or 10 min after shifting from 25°C to 34°C (Figures 4C and 4D). Surprisingly, we noted that temperature itself affected E-cad turnover—in wild-type wings, raising the temperature to 34°C increases the minute-timescale recovery fraction F_m at the expense of the immobile pool (Figures 4D and S4C). In contrast, raising the temperature of shi^{ts} to 34°C decreased F_m and increased the immobile pool (Figures 4D and S4C). Thus, endocytic recycling most likely contributes to the pool of E-cad delivered to cell junctions over minute timescales. This idea is supported by our previous observation that both dynamin and Rab11 are required to maintain a normal distribution of E-cad at *adherens* junctions specifically at this stage of wing development [30]. These experiments also suggest that dynamin-dependent endocytosis and recycling of E-cad increases with temperature.

Next, we investigated whether the endocytosis-dependent pool of E-cad was regulated by mechanical stress. We first compared mechanical stress in wild-type and shi^{ts} mutant wings at 22 hAPF and at 32 hAPF. We performed these experiments both at the permissive temperature (25°C) and 10 min after shifting to the restrictive temperature (34°C). Neither temperature nor blocking endocytosis altered mechanical stress at these
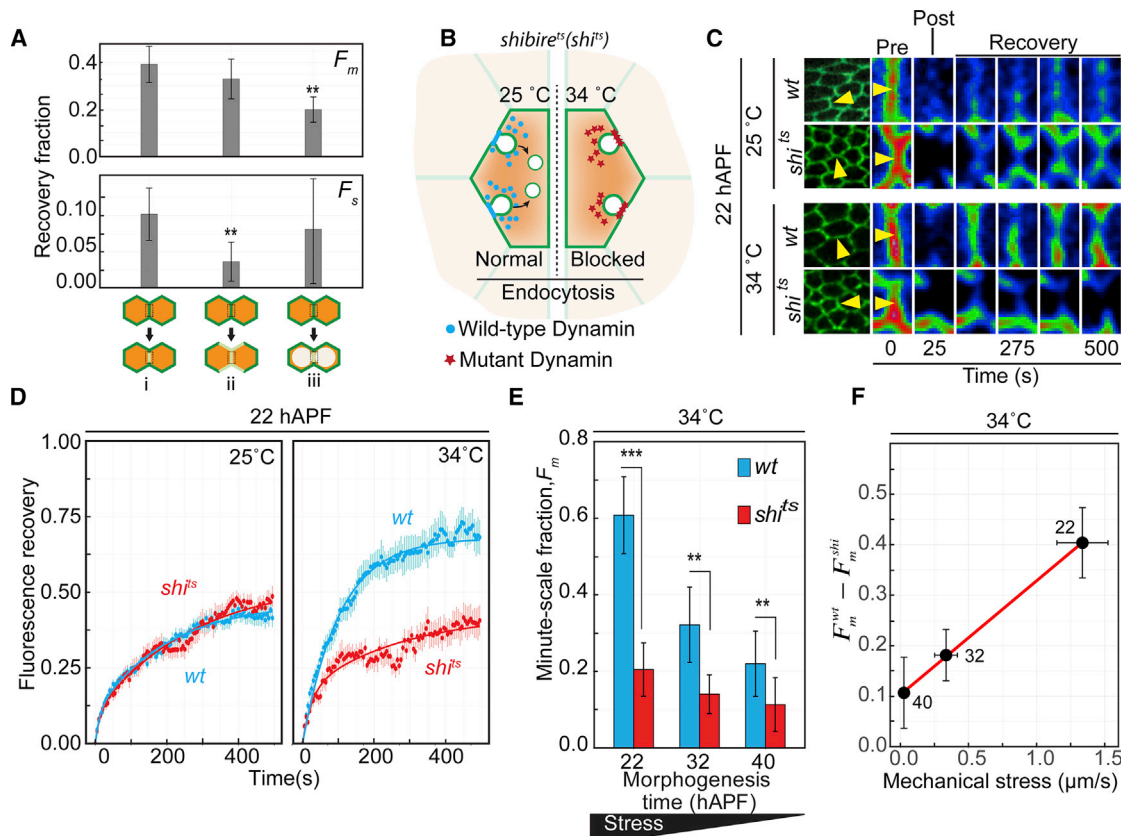
Figure 4. Mechanical Stress Modulates Endocytosis-Mediated E-cadherin Turnover

(A) Minute-scale and second-scale recovery fractions when a single junction is bleached (i), a junction and all its nearest neighbors are bleached (ii), or a junction and the cytoplasm of the contributing cells are bleached (iii). Error bars, SEM. **p < 0.01. p values are estimated with respect to single-junction bleach (I; n ≥ 15 junctions in each case). The p values are estimated by Student's t test.

(B) Schematic shows endocytosis block in a temperature-sensitive dynamin mutant, shi^{ts}, upon temperature shift. Wild-type dynamin is shown by blue circles, and mutant dynamin is shown by red stars.

(C) Time-lapse images from the FRAP time series for WT and shi^{ts} at 25°C and 34°C shows the pre-bleach, post-bleach, and recovery frames. The experiments were performed at 22 hAPF. Yellow arrowheads indicate the junctions that are bleached.

(D) FRAP curves at 22 hAPF for WT (blue) and shi^{ts} (red) imaged at 25°C (left panel) and 34°C (right panel). Error bars, SEM (n ≥25 junctions in each case).

(E) Minute-scale recovery fraction, F_m in WT (blue bars), and shi^{ts} (red bars) at 22, 32, and 40 hAPF. Error bars, SEM. **p < 0.01 and ***p < 0.001 (n ≥ 25 junctions in each case). The p values are estimated by Student's t test.

(F) Plot of difference in F_m between WT and shi^{ts} at 34°C, against mechanical stress, estimated by recoil velocity. Red solid line is the linear fit to the data, and r = 0.96 is the Pearson correlation coefficient. Error bars, SEM.

See also Figure S4.

developmental times (Figure S4F). To examine the influence of mechanical stress on the endocytosis-dependent pool of E-cad, we performed FRAP analysis 10 min after shifting wild-type or shi^{ts} mutant wings to 34°C at different times of morphogenesis (22–40 hAPF). The difference between F_m in wild-type and shi^{ts} at 34°C, a measure of the contribution of endocytosis to F_m, significantly decreased with the decrease in mechanical stress between 22 and 40 hAPF (Figures 4E, 4F, and S4E). In contrast, F_s did not change significantly (Figure S4C). Thus, mechanical stress modulates the fraction of E-cad that turns over through endocytosis (Figure 4F).

E-cadherin Endocytic Regulator p120-Catenin Shows Mechanosensitive Binding to E-cadherin

Because mechanical stress increases endocytic turnover of E-cadherin, we investigated whether this relation is controlled by the endocytic regulator p120-catenin (p120). p120-catenin binds the juxta-membrane domain of E-cadherin, where it interferes with binding of endocytic adaptor proteins and stabilizes E-cadherin-mediated adhesion [32–36]. We therefore examined whether tissue stress might alter the localization of p120. We used immunostaining to label endogenous p120 in the pupal wing epithelium at different stages of morphogenesis (Figure 5A). We estimated the junctional enrichment of p120 as the ratio between junctional and cytoplasmic p120 intensities (Figure 5B). We observed that p120 is enriched at junctions at 8 hAPF, before the onset of mechanical stress (Figures 5A and 5C). When mechanical stress peaks at 20 hAPF, p120 is predominantly cytoplasmic. It then gradually becomes enriched at junctions as mechanical stress decreases between 20 and 32 hAPF (Figures 5A–5C). These data suggest that mechanical stress inhibits the localization of p120 to the junctional region and promotes its
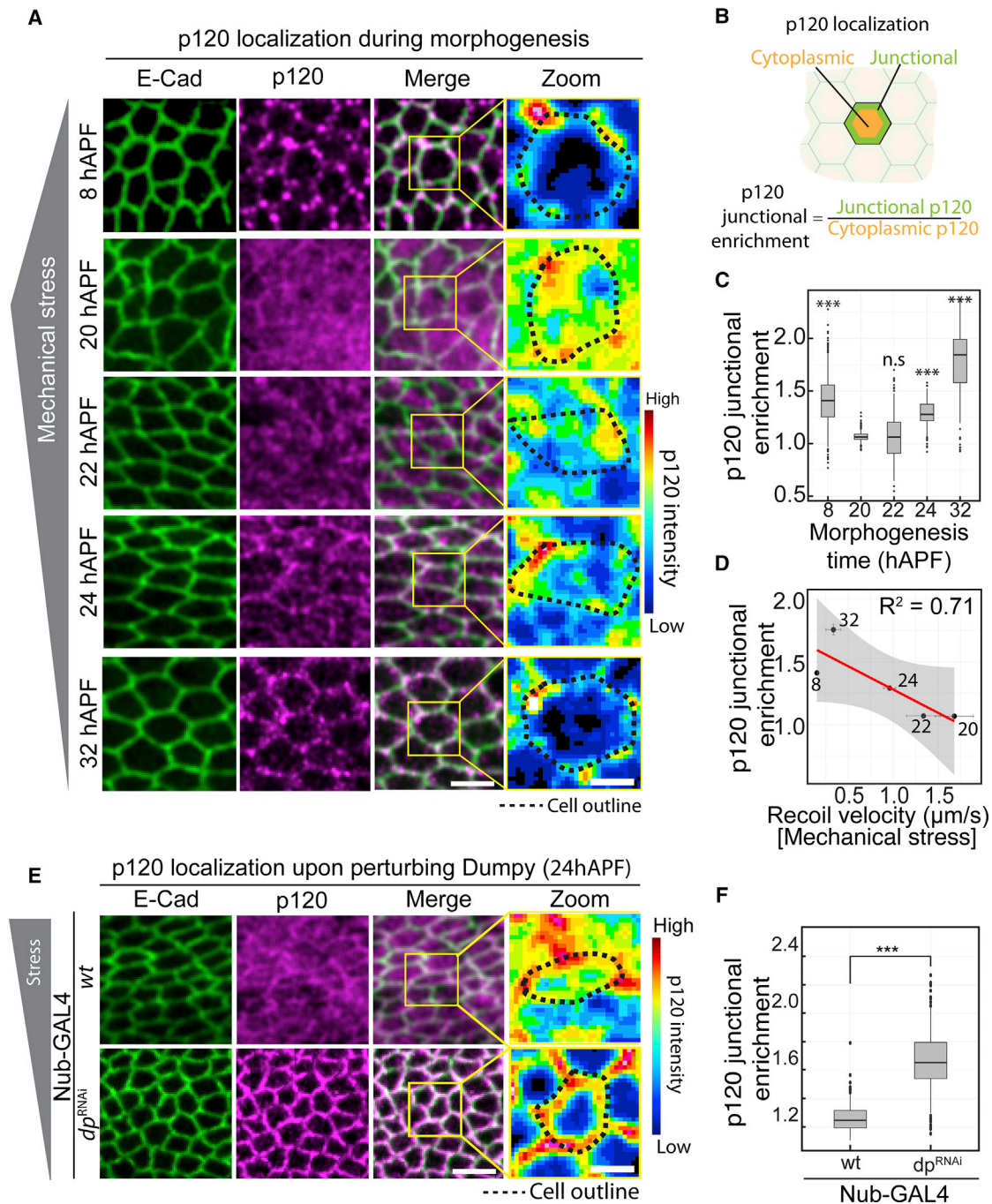
Figure 5. E-cadherin Endocytic Regulator p120-Catenin Shows Mechanosensitive Binding to E-cadherin

(A) E-cad (green), p120 (magenta), and merge images of the pupal wing at 8, 20, 22, 24, and 32 hAPF stages of wing morphogenesis. The region marked by yellow ROI in the merge image is enlarged to show the color-coded p120 intensity. Dotted line indicates the cell outline. Scale bar, 5 μm. Scale bar in zoom, 2 μm.

(B) Schematic shows the estimation of junctional (green) and cytoplasmic (orange) pools of p120 in the cell. The enrichment of p120 in the junctions is estimated as the ratio of p120 intensity in the junctions to the cytoplasm (p120 junctional enrichment).

(C) Boxplot shows the p120 JC-ratio for WT at different stages of pupal wing morphogenesis. **p < 0.01, and ***p < 0.001 (n ≥ 100 cells in each case). The p values are estimated by Student's t test.

(D) Mechanical stress (recoil velocity) versus p120 junctional enrichment graph for different stages of morphogenesis. Numbers beside the points indicate time in hAPF. Error bars represent SEM.

(E) E-cad (green), p120 (magenta), and merge images of the pupal wing when wild-type is driven by Nub-GAL4 (top panel) or dp^{RNAi} is driven by Nub-GAL4 (bottom panel). The region marked by yellow ROI in the merge image is enlarged to show the color-coded p120 intensity. Dotted lines indicate the cell outline. Scale bars, 5 μm.

(F) Boxplot shows the p120 junctional enrichment in Nub-GAL4>w- and Nub-GAL4>dp^{RNAi} wings. ***p < 0.001 (n ≥ 250 cells in each case).
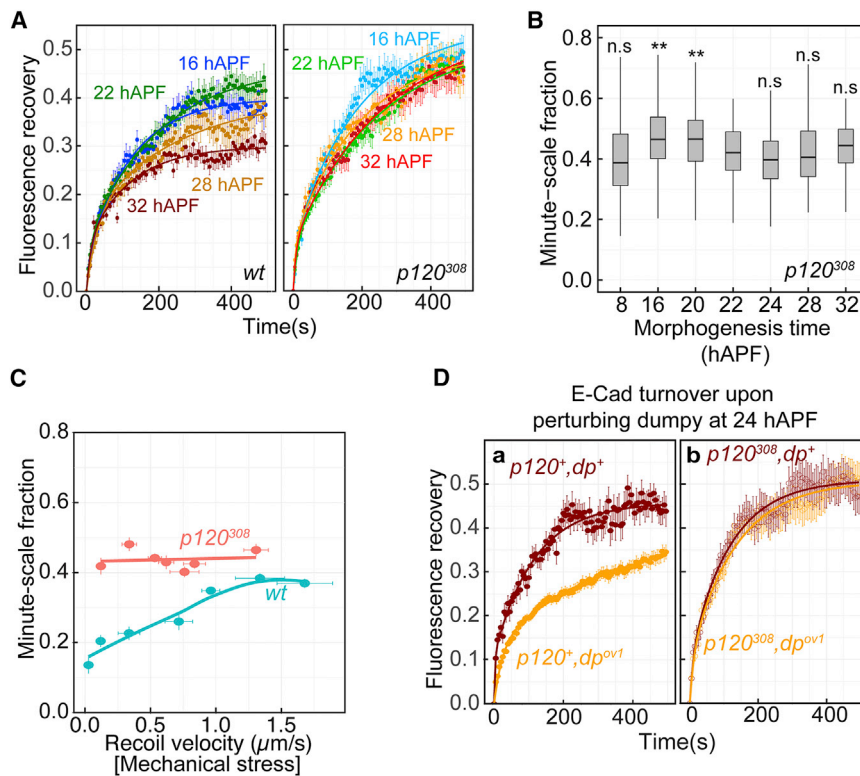
Figure 6. Mechanosensitivity of E-cadherin Turnover Is Lost in p120 Mutant Wings

(A) E-cadherin turnover in wild-type (p120+; a) and $p120^{308}$ mutant (b) during morphogenesis. Solid lines indicate double exponential fits. Error bars, SEM (n ≥ 30 junctions in each case).

(B) Boxplot shows the minute-scale recovery fraction, F_m, for $p120^{308}$ during morphogenesis. **p < 0.01 (n ≥ 30 junctions in each case). Significance for each time point is estimated in comparison with 22 hAPF.

(C) Minute-scale recovery fraction versus mechanical stress (recoil velocity) graph for $p120^{308}$ mutant (red) and wild-type, p120+ (blue). Solid line indicates the locally weighted smoothening of the data. Error bars, SEM.

(D) (a) E-cadherin turnover in wild-type (p120+, dp+) shown in brown and dp^{ov1} mutant (p120+, dp^{ov1}; orange). (b) E-cad turnover in p120 mutant in wild-type background ($p120^{308}$, dp+) is shown in brown open circles, and p120 mutant in dumpy mutant background ($p120^{308}$, dp^{ov1}) is shown in orange open circles. Solid lines indicate double exponential fits. Error bars, SEM (n ≥ 35 junctions in each case).

See also Figure S5.

scale fraction of E-cadherin turnover is lower than in wild-type due to reduced tissue stress (Figures 6D and S5B). When p120 is removed from dumpy mutant wings ($p120^{308}$, dp^{ov1}), E-cad turnover returns to wild-type levels (Figures 6D and S5A), despite the low mechanical stress in $p120^{308}$, dp^{ov1} double mutant wings (Figure S5B). Taken together, these data show that p120 makes E-cad turnover mechanosensitive.

p120-Catenin Influences the Viscoelastic Properties of the Wing Epithelium

In the pupal wing, anisotropic mechanical stress at early times promotes cell elongation together with AP-oriented cell rearrangements. At later times, cell rearrangements reorient along the proximal distal axis, which permits stress relaxation and implies viscoelasticity of the wing tissue [3]. We wondered whether the p120-dependent mechanosensitivity of E-cadherin turnover might influence how these cell dynamics respond to mechanical stress. We first investigated the relationship between mechanical stress and cell elongation in $p120^{308}$ mutant wings and compared it to that of wild-type. We used laser ablation to infer the emergence and relaxation of stresses in $p120^{308}$ mutant wings, measuring cell elongation in the corresponding wing areas before laser ablation. These experiments revealed that mechanical stress during morphogenesis is indistinguishable between wild-type and $p120^{308}$ mutant wings (Figure 7A). However, cell shape in $p120^{308}$ mutants responds more rapidly to changes in mechanical stress (Figure 7B). In $p120^{308}$ wings, the delay between the peaks of mechanical stress and cell elongation is only ~2 h, compared to 8 h in wild-type (Figures 7C and S5D). Furthermore, stress-cell deformation curves enclose a smaller area than wild-type, indicating a lower cell shape viscosity as compared to wild-type (Figure 7D).

localization to the cytoplasm (Figure 5D). To more directly assess whether mechanical stress changes p120 subcellular localization, we compared wild-type wings with wings subjected to dumpy RNAi, where mechanical stress is significantly reduced. Although p120 is predominantly cytoplasmic in wild-type wings, it is highly enriched in junctions in dumpy RNAi wings of the same stage (Figures 5E and 5F). This confirms that association of p120 with the junctional region is mechanosensitive.

Mechanosensitivity of E-cadherin Turnover Is Lost in p120 Mutant Wings

To investigate whether the stress dependence of E-cadherin turnover depended on p120, we performed FRAP analysis of E-cad in a p120-null mutant ($p120^{308}$) [33, 37]. In wild-type wings, the minute-scale recovery fraction decreases as mechanical stress decreases during morphogenesis (Figures 6A and S5). In contrast, in $p120^{308}$ wings, the minute-scale recovery fraction remains high during morphogenesis (Figures 6A, 6B, and S5). To quantitatively visualize the effect of p120 on stress-dependent E-cad turnover, we plotted the minute timescale fraction of E-cad turnover as a function of mechanical stress in wings that were mutant or wild-type for p120. In wings that are wild-type for p120, there is a strong correlation between mechanical stress and the minute-timescale fraction (Figure 6C). This correlation is strongly reduced when p120 is lost (Figure 6C). This suggests that p120 is required to stabilize E-cad at low mechanical stress, thereby making E-cad turnover stress dependent. To investigate this possibility further, we asked whether p120 was responsible for the increased stability of E-cad in dumpy mutant wings. In dumpy mutant wings that are wild-type for p120, the minute-
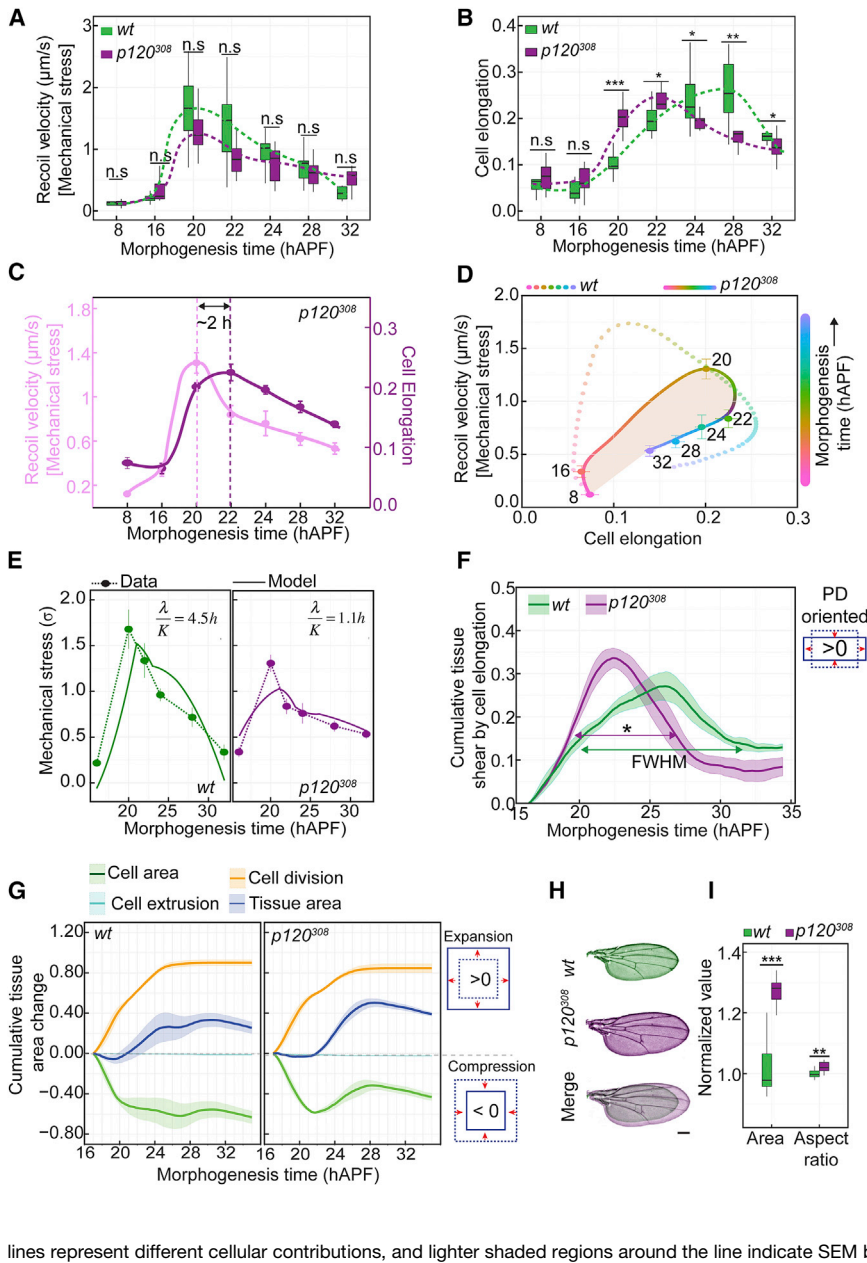
Figure 7. p120-Catenin Influences the Viscoelasticity of Wing Epithelium

(A) Boxplot showing the recoil velocity during morphogenesis for WT (green) and $p120^{308}$ (magenta). n.s. indicates that the differences are not significant, estimated by Mann-Whitney U test (n > 7 ablations in each case).

(B) Boxplot showing the cell elongation for WT (green) and $p120^{308}$ (magenta) during morphogenesis. ***p < 0.001, **p < 0.01, and *p < 0.05. The p values are estimated through Mann-Whitney U test (n > 7 ablations in each case).

(C) Plot showing the emergence of mechanical stress (recoil velocity; light magenta) and cell elongation (magenta) during pupal wing morphogenesis. Dotted vertical lines show the peaks of mechanical stress and cell elongation separated by 2 h. Error bars, SEM.

(D) Scatterplot between cell elongation and recoil velocity (mechanical stress). The numbers beside the data points are the morphogenesis time in hAPF. The solid smooth line joining the dots shows the temporal evolution of the mechanical stress and cell elongation. The color code in the line corresponds to the morphogenesis time in hAPF. The dotted color-coded line shows the temporal evolution of mechanical stress and cell elongation in *wt*. Error bars, SEM.

(E) Comparison of mechanical stress (σ) obtained from laser ablation experiments (filled circles connected by dotted line) and calculated using the Kelvin-Voigt model from 2nd order spline interpolation of cell elongation (solid line). Data for wild-type and $p120^{308}$ are shown in left and right panels, respectively. Error bars, SEM.

(F) Cumulative proximal-distal (PD) tissue shear due to cell elongation in WT (green) and $p120^{308}$ (magenta) of a region of the pupa between the 3rd and 4th longitudinal vein and around the 2nd and 3rd sensory organ from the distal tip. Lighter shaded regions around the line indicate the SEM between the wings (n = 4 wings per genotype). Double-headed arrow indicates the full width at half maximum (FWHM) of the tissue shear curve for WT (green) and $p120^{308}$ (magenta). * on the magenta arrow indicates p < 0.05 estimated by Mann-Whitney U test.

(G) Cumulative tissue area change in WT (left panel) and $p120^{308}$ (right panel). Colored solid lines represent different cellular contributions, and lighter shaded regions around the line indicate SEM between the wings (n = 4 wings per genotype).

(H) Images of adult wing of WT (green), $p120^{308}$ (magenta), and merge. Scale bar, 200 μm.

(I) Boxplot shows normalized area and aspect ratio of the blade in WT (green) and $p120^{308}$ (magenta). Normalization was performed with respect to the average value for *wt*. ***p < 0.001 and **p < 0.005, estimated by Student's t test (n > 25 wings for each case).

See also Figures S5, S6, and S7 and Videos S1, S2, and S3.

To quantitatively compare the viscoelastic properties of wild-type and *p120* mutant cells, we first asked whether the relationship between stress and cell shape could be described by the Kelvin-Voigt model. In this model, mechanical stress is given by

$$\tilde{\sigma} = K\tilde{Q} + \lambda \frac{d\tilde{Q}}{dt}, \qquad \text{(Equation 2)}$$

where K is the cell shear elastic modulus, λ is the cell shape viscosity, and $\tilde{Q}$ is cell elongation. We calculated the predicted mechanical stress using experimental cell elongation data as a function of time for both wild-type and $p120^{308}$ mutant cells. We varied λ/K and fitted the predicted mechanical stress using Equation 2 to the experimental laser ablation data. For both wild-type and *p120* mutants, we identified values of λ/K for which the calculated stress qualitatively matched the stress observed in experiments, suggesting that the Kelvin-Voigt model can account for the observed viscoelastic behaviors (Figures 7E and S6A). Interestingly, the viscoelastic relaxation time (λ/K) was larger for wild-type (4.5 h) as compared to $p120^{308}$ (1.1 h; Figures 7E and S6A). This suggests that cell shape viscosity in $p120^{308}$ is

lower than wild-type. These relaxation times can be compared to the time intervals between the peaks of stress and cell elongation, which are 8 h in wild-type and 2 h in *p120* mutants (Figures 1I and 7C). The differences in time intervals may arise from additional contributions of cell rearrangements to tissue dynamics.

To investigate whether loss of p120 might also affect other aspects of stress-dependent cell dynamics, we performed long-term time-lapse imaging in wild-type and *p120308* mutant pupal wings. We measured the cell dynamics in the same wing sub-region where we had previously inferred mechanical stress and quantified E-cadherin turnover. We segmented and tracked cells in this sub-region between 16 and 36 hAPF and quantified how this region changes its shape and area over time (Video S1). We decomposed these changes into contributions from cell rearrangements (T1 transitions), cell shape changes, cell divisions, cell extrusions, and correlation effects [3, 18]. Figure S6C shows the cumulative tissue shape change (tissue shear) and its cellular contributions in the analyzed region of wild-type and *p120308* mutant wings. Here, positive values indicate shear along the PD axis, and negative values represent shear along the antero-posterior axis (AP axis). The analyzed region in wild-type wing elongates proximo-distally over time. The cell dynamics that contribute to tissue shape change in this region are qualitatively similar to those previously described for the whole wing [3], where we showed that both active and mechanical-stress-dependent cell dynamics contribute to tissue shear in the wing. PD mechanical stress caused by hinge contraction initially elongates cells in the PD axis. Cells elongate even further in the PD axis as a consequence of active AP-oriented T1 transitions that occur during phase I of morphogenesis. T1 transitions later respond to PD mechanical stress by reorienting toward the PD axis. As PD-oriented T1 transitions generate shear along the PD axis, cell shapes partially relax. Thus, both cell elongation and T1 transitions contribute to PD shear by the end of morphogenesis. Here, in the analyzed sub-region, we have highlighted the differences in specific cellular contributions to shear in wild-type and *p120308* mutant (Figures 7F and S6B). Both cell elongation and T1 transitions contribute similarly to the PD tissue shear in wild-type and *p120308* mutant wings, and hence, the final cumulative tissue shear in *p120308* mutant is not significantly different from wild-type (Figure S6C). However, the rates at which cell elongation and T1 transitions deform the tissue are different. In *p120* mutant wings, cell elongation peaks earlier than in wild-type (Figure 7F), consistent with the smaller time delay between the peaks of mechanical stress and cell elongation that we showed earlier (Figures 1I and 7C; Video S3). Interestingly, T1 transitions in *p120* wings also reorient toward the PD axis earlier than in wild-type (Figure S6B). This suggests that tissue stresses reorient T1 transition faster than in wild-type, possibly due to faster cell shape changes.

Next, we compared the dynamics of tissue area changes in wild-type and *p120308* mutant tissue. We previously showed that the area of the whole wild-type pupal wing is fairly constant during morphogenesis because increase in tissue area due to cell divisions is balanced by cell extrusions and decrease in cell areas [17]. Analyzing vein and intervein regions separately showed that veins reduce their area overall but that this area reduction is balanced by an increase in the area of the interveins [17]. These differences between veins and interveins are largely due to differences in cell area changes. Area changes in the wild-type intervein region we analyze here are consistent with these previous findings (Video S2). Interestingly, cell areas in *p120308* mutant wings, but not wild-type wings, begin to increase at about 22 hAPF. This is shortly after anisotropic mechanical stress in the tissue peaks in both wild-type and *p120* mutants (20 hAPF; Figure 7G; Video S2). Analysis of circular laser cuts revealed no differences in isotropic stresses in wild-type and *p120* mutants at 20 hAPF (Figure S6D). By the end of morphogenesis, both cell areas and tissue area increase significantly more in *p120308* than in wild-type (Figure 7G). This may suggest that the response of *p120* mutants to isotropic stress differs from that of wild-type. Alternatively, loss of p120 may alter preferred cell area after 20 hAPF.

Our analysis of tissue shear does not predict a shape difference between wild-type and *p120308* adult wings, but the tissue area change predicts that wing area should be larger in *p120308* than in wild-type. Indeed, we observed that, although in *p120308* the major-minor axis ratio (aspect ratio) is only marginally larger than wild-type (~2.5%), the area of *p120308* adult wings is substantially larger than wild-type (~25%; Figures 7H and 7I). To test whether the observed increase in the adult wing size was due to *p120* mutation in the wing blade during pupal development, we performed time-controlled dsRNA-mediated knockdown of p120 in either the blade or the hinge region. Knocking down p120 only in the blade throughout development, or specifically during pupal stages, caused a significant increase in adult wing area (Figures S6E and S6G). In contrast, p120 knockdown in the blade during larval stages did not affect wing size (Figures S6E and S6G). Hinge-specific knockdown of p120 had no consequences for wing area and aspect ratio (Figures S6F and S6H). None of these p120 knockdown experiments showed a significant increase in aspect ratio that we observed in *p120308* mutant (Figures S6E–S6H). These data are consistent with the analysis of cell dynamics in *p120308* mutant wings and suggest that *p120* acts in the wing blade during pupal stages to affect wing size. Taken together, our findings suggest that the altered cell shape viscosity of *p120308* mutant pupal wing tissue promotes faster deformation but does not affect final wing shape. However, loss of p120 in the blade during pupal morphogenesis has enduring consequences for the final area of adult wings.

DISCUSSION

Epithelial tissues can exhibit distinct responses to applied stresses [38]. In some cases, E-cadherin-mediated adhesions are strengthened in response to stress [39], and in other cases, they are destabilized [25]. The molecular mechanisms that underlie stress-dependent strengthening are well studied and involve stress-dependent unfolding of α-catenin and vinculin that leads to enhanced linkage to cytoskeleton [22–24]. However, less was known about the mechanisms that destabilize E-cadherin. Such stress-dependent changes in E-cadherin-mediated adhesion could affect tissue fluidity or tissue stiffness. Understanding how cells tune the response of E-cadherin to mechanical stress is therefore important to understand how tissues deform and remodel in response to mechanical stress during morphogenesis. Here, using the *Drosophila* pupal wing as a model system, we have shown that the release of p120-catenin

CellPress

from *adherens* junctions under mechanical stress promotes turnover of E-cadherin complexes and decreases epithelial cell shape viscosity and speeds the reorientation of cell rearrangements with the stress axis during morphogenesis (Figures S7A and S7B).

Previous studies have shown that p120 inhibits endocytosis of E-cadherin and it is necessary to maintain the levels of E-cadherin on the membrane [40]. But the influence of mechanical stress on p120 was unknown. Here, we have identified a novel role for p120 as a part of a mechanotransduction pathway where p120 dissociates from junctions under mechanical stress (Figure S7C). How does mechanical stress cause p120 to dissociate from *adherens* junctions? One possibility is that mechanical stress-dependent signals produce post-translational modifications of p120 that alter its affinity for the E-cadherin tail. p120-Catenin can be phosphorylated by a variety of kinases that alter its activity [41–43]. Alternatively, mechanical-stress-dependent conformational changes in the E-cadherin cytoplasmic tail might reduce its ability to bind p120. If p120 is released by mechanically induced unfolding of the E-cadherin tail, this would most likely require linkage to the actin cytoskeleton via unfolding of α-catenin and vinculin. Interestingly, it is precisely these interactions that are required to strengthen E-cadherin-mediated adhesion in response to stress. This may suggest that stress-dependent internalization could result when forces are exerted for longer times or at higher levels than those required to induce strengthening.

How does release of p120 decrease cell shape viscosity? p120-catenin can bind to the E-cadherin cytoplasmic tail, and when it does so, it masks binding sites for the endocytic machinery [35]. Consistent with this, we find that mechanical stress increases the pool of E-cadherin undergoing endocytic turnover. Faster turnover of E-cadherin may facilitate cell shape changes and cell rearrangements, reducing epithelial viscosity upon dissociation of p120. Given the important role of E-cadherin in organizing the cytoskeleton at cell junctions, we would also expect such changes to have a significant impact on the cytoskeleton. p120-catenin might also impact cell shape viscosity and changes in cell area through direct effects on actomyosin dynamics. When p120 is not bound to E-cadherin, it is known to modulate the activity of Rho family proteins and the actin cytoskeleton through its interactions with RhoGEF [44–46]. This would be consistent with the observed role for actin turnover in E-cadherin stability and the viscosity of cell shape [47, 48].

Our findings show that changes in the level of p120 alter cell shape viscosity. In the future, it will be interesting to explore whether p120 levels or activity might be used to tune the viscoelastic properties of different tissues during morphogenesis. This might be important in cases where tissues deform at different rates. For example, during *Drosophila* gastrulation, the germband changes its length by 2.5-fold over the course of an hour [49], although the *Drosophila* pupal wing requires 18 h to undergo a smaller deformation. Furthermore, regulating patterns of tissue viscoelasticity could influence the shape that emerges when developing tissues are subjected to mechanical stress.

In conclusion, our findings reveal that mechanosensitive E-cadherin turnover through p120-catenin helps determine tissue viscoelasticity. These findings provide new approaches to study how interplay of tissue material properties and cell biological processes contribute to shape tissues during development and morphogenesis.

STAR★METHODS

Detailed methods are provided in the online version of this paper and include the following:

- KEY RESOURCES TABLE
- CONTACT FOR REAGENT AND RESOURCE SHARING
- EXPERIMENTAL MODEL AND SUBJECT DETAILS
  - Fly stocks and crosses
- METHOD DETAILS
  - Laser ablation experiments
  - Fluorescence recovery after photobleaching (FRAP) experiments
  - Temperature Shifts
  - Immunofluorescence staining and imaging of p120-Catenin
  - Long-term time-lapse imaging
- QUANTIFICATION AND STATISTICAL ANALYSIS
  - Analysis of laser ablation
  - Particle image velocimetry (PIV)
  - Analysis of cell elongation
  - FRAP Analysis
  - Bootstrapping parameter estimation
  - Analysis of p120 localization
  - Long-term time-lapse image analysis
  - Fitting the Kelvin-Voigt model to the stress and cell elongation data
  - Statistical tests

SUPPLEMENTAL INFORMATION

Supplemental Information includes seven figures, one table, and three videos and can be found with this article online at https://doi.org/10.1016/j.cub.2019.01.021.

AUTHOR CONTRIBUTIONS

K.V.I., F.J., and S.E. conceived and designed the project. S.E. and F.J. supervised the project and participated in data analysis. K.V.I. carried out the genetic crosses, FRAP experiments and data analysis, antibody staining, and imaging. K.V.I. and R.P.-G. performed laser ablations and data analysis. K.V.I. and R.P.-G. performed long-term time-lapse imaging and segmentation. R.P.-G. performed analysis of long-term time-lapse videos. K.V.I. and R.P.-G. developed the methods and scripts for data analysis. F.J. and J.P. developed the model, and J.P. performed the simulations. K.V.I., S.E., and F.J. wrote the manuscript.

CellPress

DECLARATION OF INTERESTS

The authors declare no competing interests.

REFERENCES

1. Blanchard, G.B., Kabla, A.J., Schultz, N.L., Butler, L.C., Sanson, B., Gorfinkiel, N., Mahadevan, L., and Adams, R.J. (2009). Tissue tectonics: morphogenetic strain rates, cell shape change and intercalation. Nat. Methods 6, 458–464.

2. Aigouy, B., Farhadifar, R., Staple, D.B., Sagner, A., Röper, J.-C., Jülicher, F., and Eaton, S. (2010). Cell flow reorients the axis of planar polarity in the wing epithelium of Drosophila. Cell 142, 773–786.

3. Etournay, R., Popović, M., Merkel, M., Nandi, A., Blasse, C., Aigouy, B., Brandl, H., Myers, G., Salbreux, G., Jülicher, F., and Eaton, S. (2015). Interplay of cell dynamics and epithelial tension during morphogenesis of the Drosophila pupal wing. eLife 4, e07090.

4. Jülicher, F., and Eaton, S. (2017). Emergence of tissue shape changes from collective cell behaviours. Semin. Cell Dev. Biol. 67, 103–112.

5. Lecuit, T., Lenne, P.-F., and Munro, E. (2011). Force generation, transmission, and integration during cell and tissue morphogenesis. Annu. Rev. Cell Dev. Biol. 27, 157–184.

6. Guirao, B., and Bellaïche, Y. (2017). Biomechanics of cell rearrangements in Drosophila. Curr. Opin. Cell Biol. 48, 113–124.

7. Heisenberg, C.-P., and Bellaïche, Y. (2013). Forces in tissue morphogenesis and patterning. Cell 153, 948–962.

8. Naganathan, S.R., Fürthauer, S., Nishikawa, M., Jülicher, F., and Grill, S.W. (2014). Active torque generation by the actomyosin cell cortex drives left-right symmetry breaking. eLife 3, e04165.

9. Munjal, A., Philippe, J.-M., Munro, E., and Lecuit, T. (2015). A self-organized biomechanical network drives shape changes during tissue morphogenesis. Nature 524, 351–355.

10. Chanet, S., and Martin, A.C. (2014). Mechanical force sensing in tissues. Prog. Mol. Biol. Transl. Sci. 126, 317–352.

11. Cross, R. (2012). Elastic and viscous properties of Silly Putty. Am. J. Physics 80, 870–875.

12. Forgacs, G., Foty, R.A., Shafrir, Y., and Steinberg, M.S. (1998). Viscoelastic properties of living embryonic tissues: a quantitative study. Biophys. J. 74, 2227–2234.

13. Kumar, S., Maxwell, I.Z., Heisterkamp, A., Polte, T.R., Lele, T.P., Salanga, M., Mazur, E., and Ingber, D.E. (2006). Viscoelastic retraction of single living stress fibers and its impact on cell shape, cytoskeletal organization, and extracellular matrix mechanics. Biophys. J. 90, 3762–3773.

14. Banks, H.T., Hu, S., and Kenz, Z.R. (2011). A brief review of elasticity and viscoelasticity for solids. Adv. Appl. Math. Mech. 3, 1–51.

15. Ray, R.P., Matamoro-Vidal, A., Ribeiro, P.S., Tapon, N., Houle, D., Salazar-Ciudad, I., and Thompson, B.J. (2015). Patterned anchorage to the apical extracellular matrix defines tissue shape in the developing appendages of Drosophila. Dev. Cell 34, 310–322.

16. Wilkin, M.B., Becker, M.N., Mulvey, D., Phan, I., Chao, A., Cooper, K., Chung, H.-J., Campbell, I.D., Baron, M., and MacIntyre, R. (2000). Drosophila dumpy is a gigantic extracellular protein required to maintain tension at epidermal-cuticle attachment sites. Curr. Biol. 10, 559–567.

17. Etournay, R., Merkel, M., Popović, M., Brandl, H., Dye, N.A., Aigouy, B., Salbreux, G., Eaton, S., and Jülicher, F. (2016). TissueMiner: a multiscale analysis toolkit to quantify how cellular processes create tissue dynamics. eLife 5, e14334.

18. Merkel, M., Etournay, R., Popović, M., Salbreux, G., Eaton, S., and Jülicher, F. (2017). Triangles bridge the scales: quantifying cellular contributions to tissue deformation. Phys. Rev. E 95, 032401.

19. Baum, B., and Georgiou, M. (2011). Dynamics of adherens junctions in epithelial establishment, maintenance, and remodeling. J. Cell Biol. 192, 907–917.

20. Takeichi, M. (2014). Dynamic contacts: rearranging adherens junctions to drive epithelial remodelling. Nat. Rev. Mol. Cell Biol. 15, 397–410.

21. Lecuit, T., and Yap, A.S. (2015). E-cadherin junctions as active mechanical integrators in tissue dynamics. Nat. Cell Biol. 17, 533–539.

22. Buckley, C.D., Tan, J., Anderson, K.L., Hanein, D., Volkmann, N., Weis, W.I., Nelson, W.J., and Dunn, A.R. (2014). Cell adhesion. The minimal cadherin-catenin complex binds to actin filaments under force. Science 346, 1254211.

23. Seddiki, R., Narayana, G.H.N.S., Strale, P.-O., Balcioglu, H.E., Peyret, G., Yao, M., Le, A.P., Teck Lim, C., Yan, J., Ladoux, B., and Mège, R.M. (2018). Force-dependent binding of vinculin to α-catenin regulates cell-cell contact stability and collective cell behavior. Mol. Biol. Cell 29, 380–388.

24. Yao, M., Qiu, W., Liu, R., Efremov, A.K., Cong, P., Seddiki, R., Payre, M., Lim, C.T., Ladoux, B., Mège, R.-M., and Yan, J. (2014). Force-dependent conformational switch of α-catenin controls vinculin binding. Nat. Commun. 5, 4525.

25. de Beco, S., Perney, J.-B., Coscoy, S., and Amblard, F. (2015). Mechanosensitive adaptation of E-cadherin turnover across adherens junctions. PLoS ONE 10, e0128281.

26. Mayer, M., Depken, M., Bois, J.S., Jülicher, F., and Grill, S.W. (2010). Anisotropies in cortical tension reveal the physical basis of polarizing cortical flows. Nature 467, 617–621.

27. Banerjee, S., Sousa, A.D., and Bhat, M.A. (2006). Organization and function of septate junctions: an evolutionary perspective. Cell Biochem. Biophys. 46, 65–77.

28. Bulgakova, N.A., Grigoriev, I., Yap, A.S., Akhmanova, A., and Brown, N.H. (2013). Dynamic microtubules produce an asymmetric E-cadherin-Bazooka complex to maintain segment boundaries. J. Cell Biol. 201, 887–901.

29. van der Bliek, A.M., and Meyerowitz, E.M. (1991). Dynamin-like protein encoded by the Drosophila shibire gene associated with vesicular traffic. Nature 351, 411–414.

30. Classen, A.-K., Anderson, K.I., Marois, E., and Eaton, S. (2005). Hexagonal packing of Drosophila wing epithelial cells by the planar cell polarity pathway. Dev. Cell 9, 805–817.

31. De Camilli, P., Takei, K., and McPherson, P.S. (1995). The function of dynamin in endocytosis. Curr. Opin. Neurobiol. 5, 559–565.

32. Davis, M.A., Ireton, R.C., and Reynolds, A.B. (2003). A core function for p120-catenin in cadherin turnover. J. Cell Biol. 163, 525–534.

33. Myster, S.H., Cavallo, R., Anderson, C.T., Fox, D.T., and Peifer, M. (2003). Drosophila p120catenin plays a supporting role in cell adhesion but is not an essential adherens junction component. J. Cell Biol. 160, 433–449.

34. Ishiyama, N., Lee, S.-H., Liu, S., Li, G.-Y., Smith, M.J., Reichardt, L.F., and Ikura, M. (2010). Dynamic and static interactions between p120 catenin and E-cadherin regulate the stability of cell-cell adhesion. Cell 141, 117–128.

35. Nanes, B.A., Chiasson-MacKenzie, C., Lowery, A.M., Ishiyama, N., Faundez, V., Ikura, M., Vincent, P.A., and Kowalczyk, A.P. (2012). p120-catenin binding masks an endocytic signal conserved in classical cadherins. J. Cell Biol. 199, 365–380.

36. Bulgakova, N.A., and Brown, N.H. (2016). Drosophila p120-catenin is crucial for endocytosis of the dynamic E-cadherin-Bazooka complex. J. Cell Sci. 129, 477–482.

37. Stefanatos, R.K., Bauer, C., and Vidal, M. (2013). p120 catenin is required for the stress response in Drosophila. PLoS ONE 8, e83942.

38. Charras, G., and Yap, A.S. (2018). Tensile forces and mechanotransduction at cell-cell junctions. Curr. Biol. 28, R445–R457.

39. Liu, Z., Tan, J.L., Cohen, D.M., Yang, M.T., Sniadecki, N.J., Ruiz, S.A., Nelson, C.M., and Chen, C.S. (2010). Mechanical tugging force regulates the size of cell-cell junctions. Proc. Natl. Acad. Sci. USA 107, 9944–9949.

40. Xiao, K., Oas, R.G., Chiasson, C.M., and Kowalczyk, A.P. (2007). Role of p120-catenin in cadherin trafficking. Biochim. Biophys. Acta 1773, 8–16.

41. Mariner, D.J., Anastasiadis, P., Keilhack, H., Böhmer, F.-D., Wang, J., and Reynolds, A.B. (2001). Identification of Src phosphorylation sites in the catenin p120ctn. J. Biol. Chem. 276, 28006–28013.

42. Alemà, S., and Salvatore, A.M. (2007). p120 catenin and phosphorylation: mechanisms and traits of an unresolved issue. Biochim. Biophys. Acta 1773, 47–58.

43. Castaño, J., Solanas, G., Casagolda, D., Raurell, I., Villagrasa, P., Bustelo, X.R., García de Herreros, A., and Duñach, M. (2007). Specific phosphorylation of p120-catenin regulatory domain differently modulates its binding to RhoA. Mol. Cell. Biol. 27, 1745–1757.

44. Noren, N.K., Liu, B.P., Burridge, K., and Kreft, B. (2000). p120 catenin regulates the actin cytoskeleton via Rho family GTPases. J. Cell Biol. 150, 567–580.

45. Grosheva, I., Shtutman, M., Elbaum, M., and Bershadsky, A.D. (2001). p120 catenin affects cell motility via modulation of activity of Rho-family GTPases: a link between cell-cell contact formation and regulation of cell locomotion. J. Cell Sci. 114, 695–707.

46. Magie, C.R., Pinto-Santini, D., and Parkhurst, S.M. (2002). Rho1 interacts with p120ctn and α-catenin, and regulates cadherin-based adherens junction components in Drosophila. Development 129, 3771–3782.

47. Engl, W., Arasi, B., Yap, L.L., Thiery, J.P., and Viasnoff, V. (2014). Actin dynamics modulate mechanosensitive immobilization of E-cadherin at adherens junctions. Nat. Cell Biol. 16, 587–594.

48. Clément, R., Dehapiot, B., Collinet, C., Lecuit, T., and Lenne, P.-F. (2017). Viscoelastic dissipation stabilizes cell shape changes during tissue morphogenesis. Curr. Biol. 27, 3132–3142.e4.

49. Irvine, K.D., and Wieschaus, E. (1994). Cell intercalation during Drosophila germband extension and its regulation by pair-rule segmentation genes. Development 120, 827–841.

50. Huang, J., Zhou, W., Dong, W., Watson, A.M., and Hong, Y. (2009). From the cover: directed, efficient, and versatile modifications of the Drosophila genome by genomic engineering. Proc. Natl. Acad. Sci. USA 106, 8284–8289.

51. Classen, A.-K., Aigouy, B., Giangrande, A., and Eaton, S. (2008). Imaging Drosophila pupal wing morphogenesis. Methods Mol. Biol. 420, 265–275.

52. Thielicke, W., and Stamhuis, E.J. (2014). PIVlab – towards user-friendly, affordable and accurate digital particle image velocimetry in MATLAB. J. Open Res. Softw. 2, e30.

53. Lowe, D.G. (2004). Distinctive image features from scale-invariant keypoints. Int. J. Comput. Vis. 60, 91–110.

54. Blasse, C., Saalfeld, S., Etournay, R., Sagner, A., Eaton, S., and Myers, E.W. (2017). PreMosa: extracting 2D surfaces from 3D microscopy mosaics. Bioinformatics 33, 2563–2569.

CellPress

STAR★METHODS

KEY RESOURCES TABLE

REAGENT or RESOURCE	SOURCE	IDENTIFIER
Antibodies		
Mouse anti-p120-Catenin monoclonal antibody	Developmental Studies Hybridoma Bank	CAT# p4B2; RRID: AB2088073
Goat anti-Mouse IgG (H+L) Cross-Adsorbed Secondary Antibody, PE-Alexa Fluor 647	Life Technologies	Cat# A-20990; RRID: AB_141581
Chemicals, Peptides, and Recombinant Proteins		
Halocarbon-700	Sigma Aldrich	CAT# 9002-83-9
Paraformaldehyde	Sigma Aldrich	CAS# 30525-89-4
Triton X-100	Serva Europe	CAS# 9036-19-5
Vectashield Antifade mounting medium	Vector Laboratories	CAT# H-1000
Experimental Models: Organisms/Strains		
D. Melanogaster: yw;DECAD^{KI}:GFP	UC School of Medicine	Kind gift from Yang Hong
D. Melanogaster: w[1110];dp^{ov1}	Bloomington Drosophila Stock Center	BDSC Cat# 276; RRID: BDSC_276
D. Melanogaster: w[1118] P{w[+mC] = PTT-GA}Nrg[G00305]	Bloomington Drosophila Stock Center	BDSC Cat# 6844; RRID: BDSC_6844
D. Melanogaster: w[1118] shi [1]	Bloomington Drosophila Stock Center	BDSC Cat# 7068; RRID: BDSC_7068
D. Melanogaster: w[1118];p120^{308}	Beatson Institute, UK	Kind gift from Marcos Vidal
D. Melanogaster: w[1118];Nub-GAL4,dp^{ov1},DECAD^{KI}:GFP	This Study	N/A
D.Melanogaster: w[1118];UAS-p120RNAi	Vienna Drosophila Resource Center	VDRC Cat# 330303; RRID:FlyBase_FBst0490992
D.Melanogaster: w[1118]; p120^{308},DECAD^{KI}:GFP	This study	N/A
D. Melanogaster: w[1118];Nub-GAL4,UAS-dpRNAi,DECAD^{KI}GFP	This study	N/A
D. Melanogaster: w[1118];p120^{308},dp^{ov1},DECAD^{KI}:GFP	This study	N/A
D. Melanogaster: w[1118];Nub-GAL4,dp^{ov1},DECAD^{KI}:GFP	This study	N/A
w[1118];shi [1],DECAD^{KI}:GFP	This study	N/A
Software and Algorithms		
ImageJ	National Institute of Health, USA	https://imagej.nih.gov/ij/index.html
MATLAB	Mathworks	https://de.mathworks.com/company/aboutus/contact_us.html#DE
Andor iQ	Oxford Instruments	https://andor.oxinst.com/products/iq-live-cell-imaging-software/
R Studio	R Studio	https://www.rstudio.com
Excel	Microsoft	https://products.office.com/en-gb/excel
Mathematica	Wolfram Research	http://www.wolfram.com/mathematica/?source=nav

CONTACT FOR REAGENT AND RESOURCE SHARING

Further information and requests for resources and reagents should be directed to and will be fulfilled by the Lead Contact, Suzanne Eaton (eaton@mpi-cbg.de).

CellPress

EXPERIMENTAL MODEL AND SUBJECT DETAILS

Fly stocks and crosses

Flies were maintained at 25°C unless specified. Male pupae were used for all experiments. Pupae at different developmental stages were used, which are mentioned in the text and figure legends. The fly strain, *yw; E-Cad::GFP* was a gift from Huang et al. [50]. The stocks of *Nrg::GFP, dp*^{ov1}*, shi*^{ts1} were obtained from Bloomington *Drosophila* Stock Center (stock ID, 6844, 279, 7068 respectively). *UAS::dp*^{RNAi} and *UAS::p120*^{RNAi} were obtained from Vienna *Drosophila* Stock Center (Stock IDs, v44029 and v330303). The fly stock *p120*^{308} was a gift from Marcos Vidal (Beatson Institute, UK). [*Nub::Gal4, E-Cad::EGFP, dp-RNAi(v44029)*], [*shi*^{ts1}*;E-Cad::EGFP*] and [*p120*^{308}*,E-Cad::EGFP*], [*p120*^{308}*,dp*^{ov1}*,ECad::EGFP*] were generated in the laboratory.

METHOD DETAILS

Laser ablation experiments

Laser ablation experiments were performed on a Zeiss microscope stand equipped with spinning disk module (CSU-X1; Yokogawa), EMCCD camera (Andor) and a custom built laser ablation system using a 355 nm, 1000 Hz, pulsed laser [26].

Circular ablation was performed with a radius of 10 μm in the region between 3rd and 4th longitudinal veins and between the 2nd and 3rd sensory organ from the distal tip of the blade. The laser was focused at equally spaced points (termed as a shot) on the ROI, with a density of 2 shots/μm. For each shot, 25 laser pulses were delivered. Since the wing epithelium has curves and undulations over an area covered by 10 μm radius circle, 5 z-planes, each 1 μm apart were ablated to ensure complete ablation of the circular ROI. In order to capture the recoil of the ablated front along the perimeter of the circular ROI, 5 z-planes, 1 μm apart were acquired with an exposure time of 50 ms and time interval of 670 ms.

Linear ablation was performed in the same region as circular ablation, with a 10 μm line oriented along the antero-posterior axis of the wing, in order to estimate the recoil along the proximo-distal axis. The ablation was done only in one single plane where the entire region of interest could be acquired in one focal plane. To capture the rapid recoil of the ablated front, single plane images were acquired with 50 ms exposure and the interval between frames was 85 ms. Initial recoil velocity of the ablated region was computed for the estimation of mechanical stress in the tissue.

Fluorescence recovery after photobleaching (FRAP) experiments
FRAP during pupal wing morphogenesis

E-Cad::EGFP line was used to perform FRAP experiments, unless specified. White pupae were collected and aged at 25°C, unless specified. Prior to the FRAP experiment, the pupal case is carefully removed using spring scissors (Fine Science Tools, Cat# 91500-09) [51]. While dissecting the pupal case, care was taken to keep the underlying wing untouched and the wing was mounted such that the central region laid flat on the coverslip. FRAP experiments were performed on an Olympus IX81 microscope equipped with a 60x 1.3 NA silicon immersion objective lens (UPLSAPO; Olympus) and a spinning disk scan head (CSU-X1; Yokogawa). Images were acquired on a back illuminated EMMCD camera (iXon DU-897BV; Andor). The region between the second and third sensory organ of the wing from the distal tip, was chosen for FRAP experiments. Multiple single junctions were selected in the field of view and the junctions were bleached using 488 nm laser at 70% power with dwell time of 50 μs and 2 iterations. Junctions were selected far apart from each other, so that only one junction per cell was bleached. 2-5 pre-bleach and 150 post bleach frames were acquired at 5 s intervals. Since the pupal wing constantly moves during morphogenesis, a 11 μm z stack was acquired centered at the bleach plane with 17 planes, 0.7 μm apart. The Z stack was maximum projected to obtain FRAP video.

FRAP combined with laser ablation

FRAP experiments with laser ablation was performed on a Zeiss Axiovert microscope equipped with a Zeiss 63X 1.3 NA water immersion objective and a spinning disc scan head (CSU-X1; Yokogawa). Images were acquired on a back illuminated EMMCD camera (iXon DU-897BV; Andor).

Temperature Shifts
Temperature shift to activate shi^{ts}

Temperature shifts were performed to activate the temperature sensitive mutant, *shi*^{ts1}, referred as shi^{ts}. Both *shi*^{ts} and WT flies were raised in 25°C. White pupae were collected and were aged till the right pupal stage at 25°C. The mutant *shi*^{ts} is inactive at the permissive temperature of 25°C, whereas its active at restrictive temperature of 34°C. So, FRAP experiments were performed in both WT and *shi*^{ts} at 25°C (control) and 34°C (experiment). Control pupae were maintained at 25°C throughout the FRAP experiment. For experiment, pupae were shifted from 25°C to 34°C at the appropriate stage of pupal development, on the microscope and incubated for 10 min, to activate the *shi*^{ts} mutation. This was followed by the FRAP experiment in either WT or in *shi*^{ts}.

Temperature shift for p120-catenin knockdown

w-; Nub-GAL4,Gal80ts, ECad::EGFP (Nub-GAL4,Gal80^{ts}) was used to perform time controlled p120 knockdown. For larval knockdown of p120, flies expressing dsRNA against p120 under UAS promotor were crossed to Nub-GAL4, Gal80^{ts} and the vials were kept

for 2 days at 25°C for egg laying. Then they were shifted to 29°C (to activate the GAL4), until the white pupal stage. Then the pupae were shifted back to 25°C until eclosion. For p120 knockdown during pupal stages, the cross was maintained at 25°C until the white pupal stage. Then the pupae were shifted to 29°C until eclosion.

Immunofluorescence staining and imaging of p120-Catenin

E-Cad::EGFP white pupae were aged at 25°C to appropriate time point and then the pupal wing were dissected in PBS [51]. In order to dissect the pupal wing, anterior and posterior parts of the pupa was cut leaving the central part intact. The pupa was carefully removed from the pupal case from the anterior opening of the pupal case. The pupa was then transferred to 8% Para-formaldehyde (PFA). While the pupa was immersed in PFA, small holes were made in the pupal cuticle for PFA to reach the pupal wing. The pupa was left in this state in PFA for 15 min. Then the cuticle was dissected and the wing was carefully removed. The entire process of wing dissection was performed in PFA within 30 min. The wings were then washed twice in PBT (PBS + 0.04% Triton X-100) for 5 min each. This was followed by incubating the wings in PBT2 (PBS + 0.2% Triton X-100) for 20 min. Then the wings were blocked in PBTN (PBT + 4% NGS) for 20 min before they were incubated in anti-p120 antibody prepared in PBTN (1:2 dilution) overnight at 4°C. The anti-p120 Catenin antibody (p4B2) was deposited to DSHB by Parkhurst, S. (DSHB, Hybridoma Product p4B2) [46]. Then the wings were washed in PBT 3 times quickly followed by 3 times for 10-15 min. Then wings were incubated in goat anti-mouse Alexa-647 secondary antibody (Life technologies) prepared in PBTN (1:500 dilution) for 4 h in a rocking platform at room temperature. The secondary antibody was removed and the wings were washed in PBT 3 times quickly followed by 3 times for 10-15 min. Then the wings were washed once in PBS. The wings were then sucked up with a 100 µL tip and transferred onto a glass slide. The wings were then mounted using Vectashield (Vector Laboratories) mounting medium and stored at 4°C. An Olympus IX83 microscope equipped with Yokogawa CSU-X1 spinning disk module was used to image the p120 immunofluorescence samples. The samples were illuminated using 488 nm laser for imaging EGFP and 638 nm laser for imaging Alexa-647. Images were acquired using 525/50 (for EGFP) and 685/40 (for Alexa-647) bandpass filters on an Andor iXON 888 Ultra EMCCD camera.

Long-term time-lapse imaging

Pupae were prepared for live imaging as previously described in FRAP experiments. Long-term time-lapse imaging was performed on an Olympus IX81 microscope equipped with Yokogawa spinning disk, a motorized *xyz* stage and Olympus UPLSAPO 60x 1.3 Sil Objective. The entire set up was encapsulated in a temperature-controlled chamber and the temperature was maintained at 25°C throughout imaging. A 488 nm diode laser was used for illumination and the emission was collected using 525/50 bandpass filter. Low laser power of 0.75 mW was used to prevent photobleaching and phototoxicity during imaging. The dorsal layer of the pupal wing was imaged using 8 overlapping image tiles in 4 × 2 configuration with 10% overlap. Each image tile containing ∼60 z sections, 1 µm apart was acquired using Andor iXon 888 Ultra EMCCD camera with an EM gain of 200 and exposure of 50 ms.

QUANTIFICATION AND STATISTICAL ANALYSIS

Analysis of laser ablation
Circular ablation

The 5 µm z stack obtained for each time frame of circular ablation was projected using the maximum projection algorithm of FIJI. An ellipse is fitted to the ablated region, either 80 s or 30 s after ablation (as mentioned in the figure legends) and the major and minor axis length and orientation were estimated. Kymographs were generated along the major and minor axis of the ellipse using a FIJI plugin (http://imagej.net/Multi_Kymograph). The initial recoil velocity, which was used as a proxy for the mechanical stress in the tissue, was estimated using a custom written routine in MATLAB (Mathworks). Recoil velocity were measured along the major and minor axis of the ellipse, represented by v_{maj} and v_{min} respectively. The orientation of the mechanical stress was estimated from the orientation of the fitted ellipse and the magnitude of recoil velocity along the major and minor axes. The isotropic (v_i) and anisotropic (v_a) recoil velocities are given by

$$v_i = \frac{v_{maj} + v_{min}}{2}; v_a = v_{maj} - v_{min} \qquad \text{(Equation 3)}$$

Linear ablation

The images obtained from the laser ablations were analyzed using Fiji and MATLAB (Mathworks). Kymographs were drawn on both sides (proximal- and distal-oriented) of the ablated line using the FIJI plugin Multi Kymograph (http://imagej.net/Multi_Kymograph). Both recoil velocities were calculated using a custom written routine in MATLAB (Mathworks). The final recoil velocity ($v_{average}$) for one ablation was computed as the average of recoil velocities that are both proximal-oriented ($v_{proximal}$) and distal-oriented recoil velocities (v_{distal}):

$$v_{avg} = \frac{v_{proximal} + v_{distal}}{2} \qquad \text{(Equation 4)}$$

CellPress

Particle image velocimetry (PIV)

Junctional displacements after linear laser ablations were analyzed by tracer particles, which in our tissues were EGFP-labeled E-Cadherin molecules. Flow fields were quantitatively measured using the open-source tool for MATLAB PIVlab [52]. The software calculated the displacement of the tracers between pairs of images (before and after the ablation) using the Fast Fourier Transformation algorithm with multiple passes and deforming windows. The interrogation areas were 32×32 px^2 and 16×16 px^2 for the first and second pass, respectively.

Analysis of cell elongation

Cell elongation in the pupal wing was estimated using the Tissue Analyzer plugin in Fiji [2]. The cell elongation for individual cells is characterized by an axis and magnitude and can be represented by a traceless symmetric tensor ε_{ij}. The tensor components $\varepsilon_1 = \varepsilon_{xx} = -\varepsilon_{yy}$ and $\varepsilon_2 = \varepsilon_{xy} = \varepsilon_{yx}$ are determined as integrals over cell area:

$$\varepsilon_1 = \frac{1}{A_c} \int_0^{2\pi} \int_0^{R(\phi)} \cos 2\phi r \, dr \, d\phi$$

(Equation 5)

$$\varepsilon_2 = \frac{1}{A} \int_0^{2\pi} \int_0^{R(\phi)} \sin 2\phi r \, dr \, d\phi$$

Here, R(ϕ) is the distance to the cell boundary at an angle ϕ. The integrals are normalized by the cell area Ac so that cell of the same shape with different areas have the same value of cell elongation. In order to estimate the average cell elongation in a region of interest (ROI), the each tensor component is averaged over all the cells in the ROI and resulting magnitude of cell elongation is given by:

$$\varepsilon = \sqrt{\langle \varepsilon_1 \rangle^2 + \langle \varepsilon_2 \rangle^2}$$

(Equation 6)

FRAP Analysis

Since the pupal wing undergoes morphogenesis, the bleached junction in the wing are in constant motion. Before computing the intensity of the junctions after photobleaching, the junctions are corrected for drift. The FIJI plugin "Linear stack alignment with SIFT" [53] was used to register each frame of the FRAP video with the previous, to remove the drift form the junctions. Only junctions which show no or very small movement with time were selected for analysis. Background was estimated from the region of the image which does not contain any junctions. Mean intensity of the bleached junctions were estimated over the entire duration of the video. Reference intensity was estimated by computing the intensity of the entire frame for all frames. Both the junction intensity and reference intensity were background subtracted and normalized by the pre-bleach intensity. The junction intensity normalized by the reference intensity to obtain the intensity corrected for bleaching during acquisition was computed as,

$$I(t) = \left(\frac{I_j(t)}{\frac{1}{N_{pre}} \sum_{N_{pre}} I_j(t)} \right) \left(\frac{\frac{1}{N_{pre}} \sum_{N_{pre}} I_r(t)}{I_r(t)} \right)$$

(Equation 7)

where $I_j(t)$ and $I_r(t)$ represent the junction intensity and reference intensity respectively and N_{pre} is the number of pre-bleach frames. This was further normalized as:

$$I_{norm}(t) = \frac{I(t) - I_{post}}{I_{pre} - I_{post}}$$

(Equation 8)

where

$$I_{pre} = \frac{1}{N_{pre}} \sum_{N_{pre}} I(t)$$

(Equation 9)

and I_{post} ist the normalized intensity immdietly after bleaching.

Bootstrapping parameter estimation

Bootstrapping procedure was used to fit the FRAP curves and estimate the recovery parameter. Toward this, 3 FRAP curves were randomly selected from the set of FRAP curves for a given experiment and their mean was estimated. A double exponential of the following form was fitted to the curve and the fitting parameters were estimated:

$$I_{Frap}(t) = F_s \left(1 - e^{-t/\tau_s} \right) + F_m \left(1 - e^{-t/\tau_m} \right)$$

(Equation 10)

where $I_{Frap}(t)$ is the normalized fluorescence intensity at time t, F_s is the second-scale recovery fraction, F_m is the minute-scale recovery fraction, τ_s is the second-scale timescale and τ_m is the minute-scale timescale. A double exponential provided the best fit to the curve (Table S1). This procedure was performed iteratively for 1000-2500 iterations to obtain a smooth distribution of the fit parameter.

Analysis of p120 localization

Localization of p120 within cells was estimated using Fiji plugins and custom written MATLAB routines. The junctional network visualized by E-Cadherin::GFP was segmented using Tissue Analyzer. A 3-pixel junctional mask (M_j) was generated for each cell and was multiplied with the p120 image to get the junctional intensity of p120 (I_{junc}). A mask of the cell cytoplasm (M_c) was generated by subtracting the mask for the junctional network from the whole cell mask. This M_c was multiplied with the p120 image to get the cytoplasmic intensity of p120 (I_{cyto}). The enrichment of p120 in junction was given by the p120 junction to cytoplasm ratio as

$$\eta_{JC} = \frac{I_{junc}}{I_{cyto}}$$ (Equation 11)

Long-term time-lapse image analysis

The 3D image tiles obtained from the imaging were projected and stitched using the processing pipeline PreMosa [54]. After the projection and stitching, a small region was cropped around the second and third sensory organ of the pupal wing between the vein L3 and L4 and the resulting images were aligned through time using the Fiji plugin "Linear Stack Alignment With SIFT" [53]. This is the same region where the laser ablations were performed. The registered images were segmented using Tissue Analyzer [2]. The analysis of cell dynamics during pupal wing morphogenesis was performed using Tissue Miner [17]. An ROI of the same size was defined at the beginning of both WT and $p120^{308}$ video using Tissue Miner [17] and the cells inside this ROI were forward-tracked throughout the whole time-lapse.

Fitting the Kelvin-Voigt model to the stress and cell elongation data

To test our hypothesis that the cell shape viscosity of the epithelial wing tissue is lower in the $p120$ mutant as compared to the wild-type, we used the Kelvin-Voigt model for the anisotropic stress given by

$$\tilde{\sigma} = K\tilde{Q} + \lambda \frac{d\tilde{Q}}{dt}$$ (Equation 12)

where, K is the cell elastic modulus, λ is the cell shape viscosity and $\tilde{Q}$ is cell elongation. We calculated the temporal derivative of Q in Mathematica (Wolfram Research) using a second order spline interpolation through the cell elongation data points. Using the spline interpolation of the cell elongation data and its temporal derivative we fit the solution of Equation 12 to the measured values of the mechanical stress. Since the measured retraction velocity is only proportional to the stress, we only give the fitted value of the ratio of cell shape viscosity to the cell elastic modulus (λ/K).

Statistical tests

Statistical tests were performed using MATLAB (Mathworks). Kolmogorov-Smirnov test was performed to test whether the observed values where normally distributed. When the distribution was normal, Student's t test was performed to estimate significance of the quantities. In case the values are not normally distributed, non-parametric Mann-Whitney U-test was performed to estimate the significance of differences between the quantities. The corresponding p values and the method used to estimate them are mentioned in the figure legends. For multiple comparisons ANOVA was performed to check the validity of significance estimated by t tests. False discovery rates (FDR) for correlations were estimated by randomly permuting the values of the quantities correlated for 30×10^3 iterations, computing the correlation coefficient for each iteration. The probability of finding a correlation greater than or equal to the observed correlation was considered as the false discovery rate.